Experimental Study of Helicopter Fuselage Drag

Robert Stepanov[1], Vladimir Zherekhov[2], Vladimir Pakhov[3], Sergey Mikhailov[4],
Kazan National Technical University (KAI), 10 Karl Marx St., Kazan, 420111, Russian Federation

Aleksey Garipov[5], Walter Yakubov[6],
JSC "Kazan Helicopter Plant", 14 Tetsevskaya St., Kazan, 420085, Russian Federation

and

George N. Barakos[7]
University of Liverpool, School of Engineering, Liverpool L69 3GH, UK.

Abstract

Experimental data are presented for the parasite drag of various helicopter fuselage components, such as skids, external fuel tanks, and tailplane. The experiments were conducted at the KNRTU-KAI T-1K wind tunnel, investigating four versions of a fuselage similar to the ANSAT helicopter. It was found that for the range of pitch angles $-10° \leq \alpha \leq 10°$, the skids added 80% to the drag of the bare fuselage, while the tailplane increased the drag by 20%. At the same conditions, external fuel tanks were found to add 48% to the clean fuselage drag. A simple rotor hub with a tail support added 74% to the bare fuselage in the range of pitch angles $-8° \leq \alpha \leq 6°$. Streamlining the rear fuselage was found to reduce the drag by 16% over the range of pitch angles $-10° \leq \alpha \leq 10°$. Apart from the parasite drag, ideas for drag reduction are also discussed.

Nomenclature

Latin

C	=	area of the exit cross-section of the nozzle, m^2
C_D	=	drag coefficient, $C_D = 2D/\rho V^2 S$
$C_{D\max}$	=	maximum value of drag coefficient C_D
C_{DS}	=	scaled drag coefficient (Equation 3)
L	=	fuselage length, m
M	=	Mach number
N	=	number of samples

[1] Junior Researcher, Department of Aerohydrodynamics; rpstepanov@kai.ru
[2] Associate Professor, Department of Aerohydrodynamics; zherehov.agd@kstu-kai.ru
[3] Junior Researcher, Department of Aerohydrodynamics; pahov.agd@kstu-kai.ru
[4] Professor, Department of Aerohydrodynamics; sergey.mikhaylov@kai.ru
[5] Chief engineer, JSC "Kazan Helocpter Plant"; garipov_ao@kazanhelicopters.com
[6] Leading expert, JSC "Kazan Helocpter Plant"; yakubov_wk@kazanhelicopters.com
[7] Professor, School of Engineering, Walker Bld., The Quadrangle; g.barakos@liverpool.ac.uk. RAeS Member, corresponding author.

S	=	characteristic area of a tested model (it remains constant for dressed and undressed configurations), which was defined as a frontal area of the clean fuselage at $\alpha = 0°$ and $\beta = 0°$, m^2
TEL	=	twin engine light
V	=	wind speed, m/s
k_0	=	constant scaling coefficient, which took the same value for each model
max	=	maximum
min	=	minimum
$\bar{x}$	=	sample mean

Greek

α	=	pitch angle (degrees)
β	=	yaw angle (degrees)
ν	=	kinematic viscosity, m^2/s
σ	=	standard deviation
φ_{hs}	=	angle of incidence of the horizontal stabilizer (degrees)
φ_{vs}	=	angle of incidence of the vertical stabilizer (degrees)

Acronyms

CF	=	clean fuselage
CF1,CF2, CF3,CF4	=	clean fuselage of models 1, 2, 3 and 4, respectively
FT1	=	type 1 fuel tank (rectangular prism shape with rounded edges)
FT2	=	type 2 fuel tank (cylindrical shape with rounded ends)
HB	=	main rotor hub
KNRTU-KAI	=	Kazan National Research Technical University named after A.N. Tupolev
MTOW	=	Maximum take-off weight
MH	=	main rotor hub
RANS	=	Reynolds-averaged Navier-Stokes equations
Re	=	Reynolds number based on the fuselage length, $Re = VL/\nu$
SK	=	skids
SK1, SK2	=	type 1 and type 2 skid configurations
TEL	=	Twin-Engine Light
TH	=	tail hub
TP	=	tailplane
TS	=	tail support
TsAGI	=	Central Aero-Hydrodynamics Institute (Russian Federation)
T-1K	=	wind tunnel at KNRTU-KAI
WT	=	wind tunnel

Subscripts

D	=	drag
DS	=	scaled drag
i	=	the number of the measured sample
hs	=	horizontal stabilizer
vs	=	vertical stabilizer

1. **Introduction**

Fuselage drag has always been of primary concern for fixed and rotary-wing aircraft. However, helicopter fuselages are less streamlined, because helicopters have the overall lower flight speed in comparison to fixed-wing aircraft, and the need to accommodate mission-specific equipment added externally to helicopters such as search lights, winches, fuel tanks etc., which significantly increase the overall drag [1]. The cost of helicopter operations and concerns over the impact of all flying machines to the environment fueled a rethink of the helicopter fuselage drag. Because most designs begin from a bare hull, it is beneficial to achieve low drag even for this simplified configuration. Higher drag will not necessarily limit the top speed of the helicopter, which is mainly dictated by the design of the main rotor, but will affect the payload versus range trades of the aircraft with operational and financial consequences.

Therefore, drag reduction is one of the main targets of modern helicopter design. The drag itself is influenced by various parameters, such as shape, roughness, free stream turbulence, boundary layer properties [1]. Its accurate prediction remains one of the most difficult challenges in aerodynamics because of the complex geometries inherent to helicopters, unsteady flowfields [2] and complex fuselage-rotor interactions [3–6].

Parasite drag reduction has become increasingly important during the last decade because of the potentially significant gains it may bring to the aerodynamic performance and the minimization of fuel consumption [7–9]. Parasite drag is the aggregate drag of parts of a helicopter (e.g., tailplane, skids, rotor head etc.), which provide no direct contribution to the main rotor lift [10]. It consists of streamline drag, where the flow closes smoothly behind the body, and the bluff body drag in which case the flow separates behind the body [11]. The total drag of a helicopter, at level cruise flight, comprises parasite drag, profile drag of rotor blades, and induced drag due to lift production [12]. The power breakdown of a typical single-rotor helicopter has shown that at cruise flight of 270 km/h, over 45% of its power is used to overcome its airframe drag [13]. References [14,15] suggest that the total drag of a typical civil utility helicopter is caused by induced drag (about 25%), viscous drag (23%), interference drag (40%, main contributor being the rotor-fuselage interaction), wave drag (10%), and other components (10%). These numbers are only indicative and can vary with the configuration, weight class and flight conditions of the helicopter.

Wind tunnel experiments are usually complemented by theoretical or numerical studies. Experiments are difficult to conduct and very expensive. This means that a considerable effort should be put into computing, which itself is limited by the availability of CFD software and computer hardware [16]. However, WT experiments provide the main validation data for CFD. An accurate interpretation of WT data, such as WT wall interference corrections [17], is of paramount importance. Furthermore, rescaling of experimental scaled conditions to flight conditions should be conducted with care so as to minimize errors [18].

Wagner [12] presented drag breakdown in percentage of total parasite drag for a typical TEL-class utility helicopter (without external fuel tanks), with a MTOW of 2.5 metric tons in level cruise flight [12], which is listed in Table 1. Grawunder *et al.* [7] carried out WT experiments and numerical computations on a similar type TEL-class helicopter, where the case with rotating rotor head, trimmed for fast level flight was investigated. Drag values for this model were slightly higher because the tailboom was truncated upstream of the stabilizer to fit the balance support. The summary of the drag breakdown is shown in Table 1.

	Level cruise flight, Wagner [12]	WT experiment, Grawunder [7]	CFD, Grawunder [7]
	-	$\propto= 0°, \beta = 0°$	$\propto= 0°, \beta = 0°$
Fuselage	38%	31%	26%
Rotating rotor head (with interference effects)	23%	38%	-
Skids (with interference effects)	13%	27%	-
Tail (with interference effects)	7%	4%	-
Tail rotor hub (with interference effects)	5%	-	-
Miscellaneous	14%	-	-
Rotating rotor head (isolated)	-	-	27%
Skids (isolated)	-	-	18%
Skids - fuselage interference	-	-	11%
Rotor head - fuselage interference	-	-	18%
Total	100%	100%	100%

Table 1. Parasite drag breakdown in percentage of total parasite drag for a typical TEL-class utility helicopters (with no external fuel tanks) [7]

According to Stroub and Rabbot [19], the total consumed power for a typical TEL helicopter in forward flight consists of the parasite power, induced power, profile power and tail rotor power. The parasite power makes up about 50 % of total power requirement.

The parasite power can be estimated as follows [7]:

$$P_p = {}^{1}\!/_{2}\, \rho A C_D V^3 \tag{5}$$

Hence, for a TEL class helicopter, the 10% reduction of parasite drag in forward flight will lead to 5% power reduction [7].

The main hub is considered to be the largest contributor to parasite drag [10], which adds up to a third of the total drag for medium and light helicopters [20]. A comprehensive summary of hub drag along with ways to minimize it, were previously presented by Sheehy [21]. Drag of the rotor head with its components having different geometries was previously investigated by Kneisch et al. [20].

Apart from the hub, the fuselage is one of the biggest parasite drag contributors, especially at high speed flight. Hence, recently there has been growing concern over accurate fuselage drag prediction [22–24].

Costes *et al.* [25] presented results of pressure distribution and force data obtained in the ONERA F1 wind tunnel (WT) for three simplified fuselage configurations of a helicopter up to real flight Reynolds numbers (from 6 to 60 million) based on fuselage lenght. The data were then compared against numerical results. Although the pressure distribution obtained by numerical methods compared well to the WT results, none of the computations could predict the total drag. This was because of the Reynolds number effect and fuselage geometry variations of three tested models. Subsequent computations which included strut interference effects improved the predictions [26, 27].

Lehman *et al.* [28] compared WT experiments of the MRH 90 helicopter fuselage with numerical data and observed poor agreement at low angles of attack and angles of sideslip, where the pressure and viscous drag components were comparable.

One of the largest drag contributors to a helicopter drag is characterized by the aft-body of helicopter fuselage due to flow separation and formation of two vortices [29]. However, quite often the shape of the fuselage aft-body cannot be easily modified due to mission requirements and design constraints. A special drag problem relates to the rear fuselage upsweep with rear loading doors, where the width of the doors should be approximately constant. Seddon [30] used wind tunnel model tests and obtained the variation of drag with upsweep angle at separate pitch angles ($-18° \leq \alpha \leq 9°$).

Zhang et al. [29] investigated the aerodynamic design of the EC135 backdoor area and presented results of numerical computations and wind tunnel experiments. Reshaping of the fuselage aft body lead to 22% drag decrease in comparison to the baseline EC135 helicopter. An additional drag reduction of 4% was achieved as a result of the backdoor geometry optimization.

Another study was carried out by Venturelli *et al.* [31], where the effect of a rear ramp of a helicopter fuselage on its aerodynamic characteristics was investigated. They presented results of multivariable CFD computations of different rear ramp shapes and fitted the obtained data using multivariate smoothing splines based on thin plates. Van Dam [32] summarized the usage of numerical methods with Euler and RANS equations to estimate the drag of helicopters and its components.

Research in fuselage drag reduction using active flow control has also been gaining momentum in recent years. Le Pape *et al.* [33] attempted to reduce fuselage drag by alleviating flow separation at the backdoor area of a helicopter (clean fuselage with no additional components and with a pronounced rear loading ramp) with active flow control. An average of 15 to 20% drag reduction was achieved. Schaeffler *et al.* [34] observed a maximum drag reduction of 22% for a 1/3 scale powered rotorcraft model, which was equipped with 8 blowing slots in the ramp section. In a similar study, Martin *et al.* [35] achieved large drag reductions (about 20%) using active flow control in the rear ramp section. They also presented a detailed study of flow topology in the ramp section.

Keeping in mind that a large portion of parasite drag is generated because of the rotor hub and fuselage, recent attention was primarily focused on rotor fuselage interaction and on rotor and hub interaction [9, 36–37]. Reß *et al.* [38] studied the effect of landing gear and a rotating rotor head in a low-speed wind tunnel, which induce approximately 80% of the total parasite drag. While studying different landing gear modifications, it was found that streamlining the cross sections of the landing gear leads to 45% lower drag compared to the baseline configuration.

A retractable landing gear significantly improves the aerodynamic characteristics, though results in weight increase [13]. A fixed landing gear produces bluff-body drag [11]. Reference [39] provides a dataset of drag coefficients for different models of wheeled landing gear.

Apart from major drag contributors, modern helicopters have small geometric features, such as antennas, door handles etc., which contribute greatly to overall drag because they operate at subcritical Reynolds numbers and hence have high drag coefficients [11].

Keys *et al.* [13] presented recommendations on parasite drag reduction, which were based primarily on wind tunnel test data. However, there seems to be a shortage of information related to parasite drag reduction of different fuselage components (skids, external fuel tanks, tailplane, etc.).

It is, therefore, important to understand the impact of each fuselage component on the overall drag and to quantify the parasite drag. Equally comparing the drag coefficient of clean and “dressed” fuselage is very important for the overall performance analysis of the helicopter. This is the objective of the present work that uses a baseline fuselage design, similar to the ANSAT helicopter (Figure 1).

Figure 1.The ANSAT helicopter produced by the Kazan Helicopter Plant in the Tatarstan Republic of the Russian Federation.

This paper addresses helicopter fuselage drag, mostly from an experimental perspective. All wind tunnel (WT) measurements were conducted at the KNRTU-KAI T1K subsonic, closed-return, open-jet tunnel. The paper begins with a survey of similar studies reported in the literature and a table is compiled comparing the various tests. Then, the geometries and configurations of the employed WT models are discussed, along with a matrix presenting the available data and the conditions they were obtained at. Then, the analysis of the parasite drag is presented. Based on the obtained results, suggestions for drag reduction are put forward and assessed. Finally, conclusions are drawn and a summary of the findings is presented with some suggestions for further studies.

2. Fuselage configurations and experimental conditions

This paper presents a summary of wind tunnel experiments carried out in the T-1K wind tunnel. All of the models were manufactured of wood or composite materials for the WT tests and made at 1:7 scale. The shapes of all four models were derived from the baseline twin engine light (TEL) ANSAT fuselage, based on an empirical design with the aim to reduce the drag because of the bluff shape inherent to helicopter fuselages while maintaining the ability to fulfil operational needs set by manufacturers. Efforts were made to collect data from most of the four configurations with or without added components.

For each case, geometric changes made to the previous models were considered. Figure 2 shows the outlines of the various designs considered in this work and table 2 compares these models. Detailed descriptions are given in Sections 2.1 through 2.4. Throughout this work, CF1, CF2, CF3 and CF4 will refer to the clean fuselages 1, 2, 3 and 4, where the numbers indicate the corresponding model.

Two different skids were used in the experiments, referred to as Type 1 (SK1) and Type 2 (SK2) skids, as shown in Figure 3. The length of the skids was 35% of the fuselage length (L). The skids for Models 1 and 4 were manufactured separately to satisfy the scale condition $0.35L$. Same skids were used for Models 1 and 2.

Figure 4 shows comparative composite views of the two models which also feature three different fuel tank shapes (FT1, FT2 and FT3).

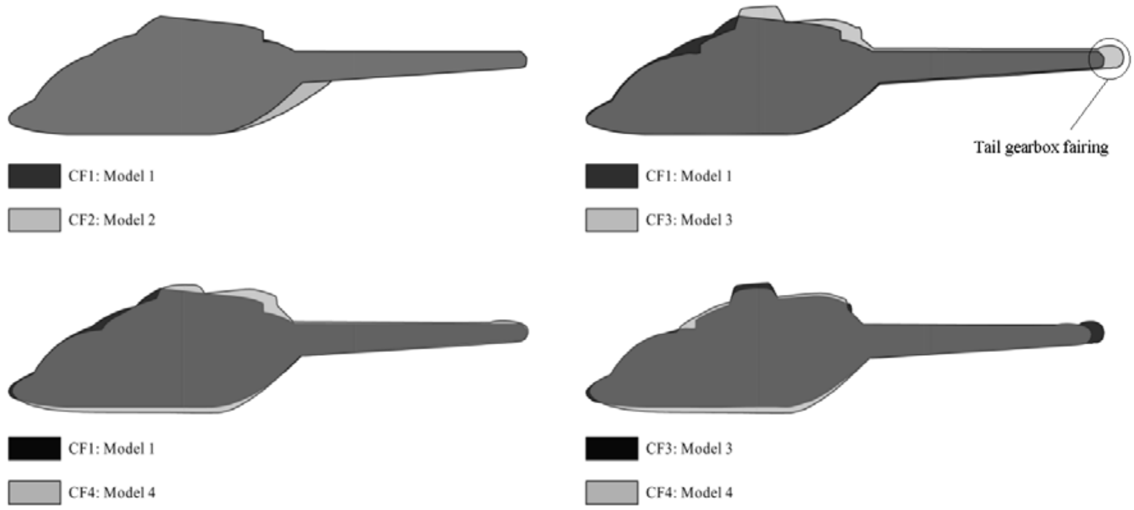

Figure 2.Side view comparison of the fuselage models

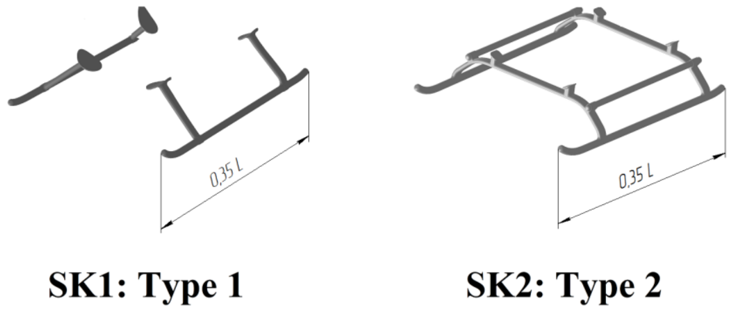

Figure 3. Two modifications of the skids

Type 1 fuel tank (FT1) had a shape of a circular cylinder with rounded ends. Fuel tank 2 (FT2) had a cylindrical shape with a rounded front and a conical rear. Type 3 fuel tank (FT1) had a shape which is close to a right rectangular prism with rounded corners. Its inner surfaces of FT1 and FT3 were made to match the shape of the fuselage. A tail support was also used for all experiments with Model 3. The tail support was of a circular cross-section with a radius of 0.34% of the CF3 fuselage length. To gain better understanding, the tail support, fuel tanks and the tailplane are shown on Figure 4.

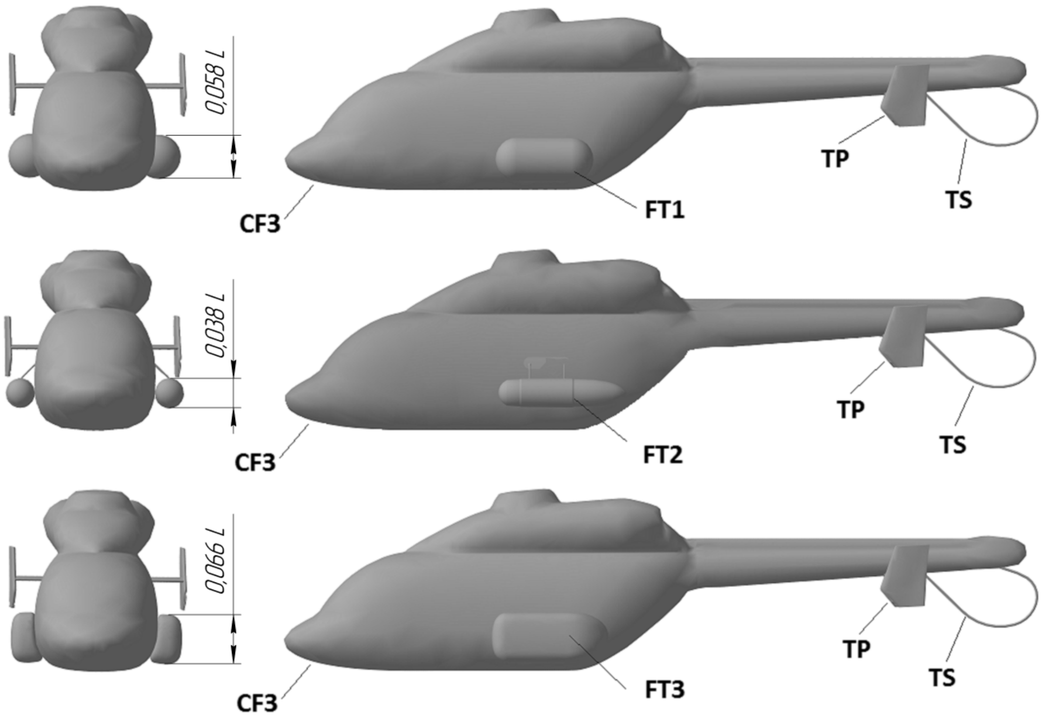

Figure 4. Side and front views of the Model 3, featuring the attachment of the fuel tanks (FT1 and FT2), tail support (TS) and the tailplane (TP) (L is the length of CF3)

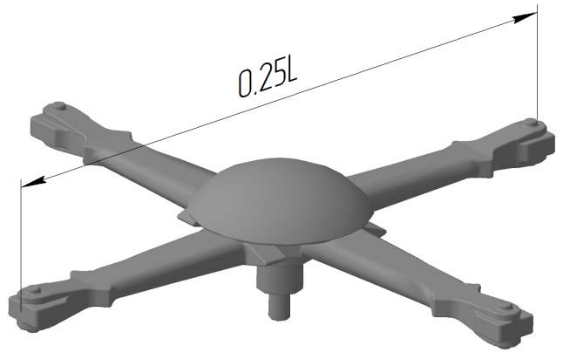

Figure 5. Main hub (MH)

The pitch angles of the tailplane's horizontal (φ_{hs}) and vertical (φ_{vs}) stabilizers relative to the fuselage reference plane for each model are also presented in Table 2. The main rotor hub (MH) was fixed to the fuselage and included the blade-root attachment beanie and main shaft. A detailed view of the MH is shown in Figure 5. It is shown that the MH diameter was approximately 25% of the fuselage length (L) of Models 2 and 3.

2.1. Model 1

The model consisted of a clean fuselage (CF1), skids (SK2), and twin-fin tailplane (TP) (refer to Figure 6).

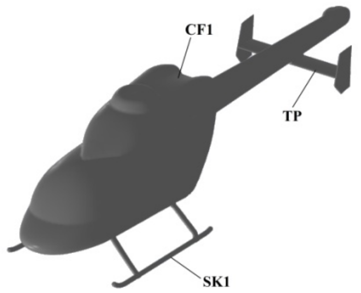

Figure 6. Schematic of Model 1

2.2. Model 2

Model 2 had the same shape as Model 1 except of the aft part of the fuselage that was extended near the rear ramp, as shown in Figure 2. MH was also added for this case.

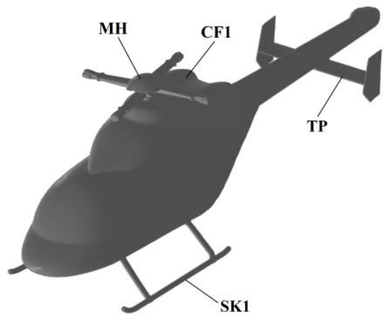

Figure 7. Schematic of Model 2

Model 2 consisted of the clean fuselage (CF2), removable skids (SK1), main rotor hub (MH) with a hub fairing, and a twin-fin tailplane (TP).

2.3. Model 3

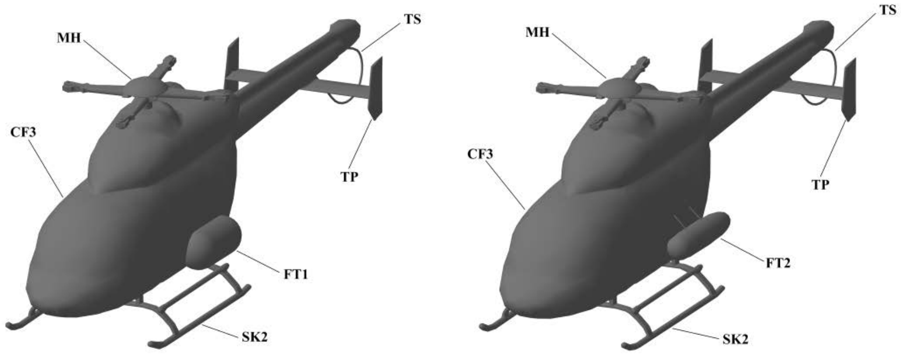

Figure 8. Schematic of Model 3

Model 3 was obtained as a result of the following modifications made to Model 1. A modified engine cowling was installed (see Figure 2) and a tail support (TS) was also added.

A tail gearbox fairing was installed, which resulted in a tail boom extension (see Figure 2). Two modifications of external fuel tanks (FT1 and FT2) were used, which were symmetrically positioned on each side of the fuselage (see Figure 8).

Model 3 consisted of the clean fuselage (CF3), tail support (TS), main hub (MH) removable skids (SK2), twin-fin tailplane (TP) and two types of external fuel tanks (FT1 and FT2).

2.4. Model 4

Compared to Model 3, Model 4 had a modified engine cowling (see Figure 2) with a more streamlined shape, lower bottom surface of the fuselage and shorter length of the tailboom with a modified shape of the tail gearbox fairing.

Model 4 consisted of the clean fuselage (CF4) and removable skids (SK1), twin-fin tailplane (TP) and external fuel tanks (FT3).

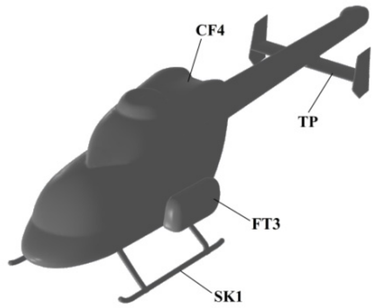

Figure 9. Schematic of Model 4

	Fuselage	**Tail support**	**Tail boom**	**Tailplane type**	**Main rotor hub**	**Skids**	**Fuel tanks**
Model 1	CF1	no	CF1	twin-fin, $\varphi_{vs} = +7^\circ$ $\varphi_{hs} = -0.5^\circ$	no	SK1	no
Model 2	CF1 + extended rear ramp	no	CF1	twin-fin, $\varphi_{vs} = +6^\circ$ $\varphi_{hs} = -0.5^\circ$	yes (hub fairing, torsion)	SK1	no
Model 3	modified (new engine cowls)	yes, added tail support (TS)	Extended due to gearbox fairing	twin-fin, $\varphi_{vs} = +7^\circ$ $\varphi_{hs} = -0.5^\circ$	yes (hub fairing, torsion)	SK2	FT1, FT2
Model 4	modified (new engine cowls, extended bottom surface)	no	CF1 + gearbox fairing	twin-fin, $\varphi_{vs} = +7^\circ$ $\varphi_{hs} = -0.5^\circ$	no	SK1	FT3

Table 2.Summary of tested models

3. Wind tunnel characteristics, measurement methods, wind tunnel corrections and processing of the raw data

3.1. Test facility

All results were obtained in a low speed WT at the Kazan National Research Technical University (KNRTU-KAI). This is a single-return, closed-circuit, open-jet WT with a contraction ratio of 4.9. The WT has a free stream turbulence intensity below 0.5% in the jet core, a nozzle exit diameter of 2.25 m, and can reach wind speeds up to 50 m/s. The tests were performed at 28, 36 and 43.5 m/s, respectively.

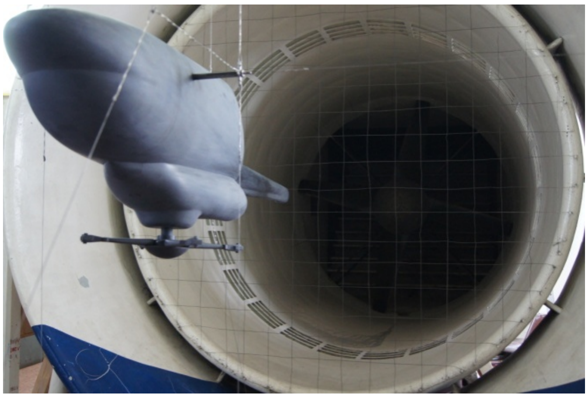

Figure 10. Model 4 fuselage in the T-1K WT at KNTRU-KAI

Strain gauge sensors, with the 16-Bit National Instruments PXI 4220 analog-to-digital converter, were used for measurements of forces and moments in a six component Prandtl-type balance [40]. In this work, the integration time for each angle was set to 60 seconds; the recorded data were then time-averaged. The strain gauge sensors were able to measure loads with a precision of 10 grams at each of all six components of the balance. The model was suspended on wires of 0.8 mm diameter, as shown in Figure 10.

Similarity parameters for low speed WTs are affected by free and solid boundaries. The jet of the WT is distorted due to the presence of the models inside the test section. Corrections for S/C ratio (S – characteristic area of a tested model, which was defined as a frontal area of the clean fuselage configuration; C – area of the exit cross-section of the nozzle), influence of the balance suspension system and suspension devices [41], flow deformation at different pitch and yaw angles and blocking-effect correction were applied to the results obtained in T-1K WT. The drag coefficient of the mounting system was determined separately (with the model removed) and subtracted from the drag coefficients of the tested model obtained earlier. The pitch angle was corrected for the effect of flow boundaries and slanting angle of the wind velocity, which is 0.2° for T-1K WT. A summary on the data analysis in the T1K wind tunnel can be found in reference [40].

It should be noted that the characteristic area of the tested model S remained constant for dressed and clean configurations, which was equal to the frontal area of the clean fuselage of each model at $\alpha = 0°$ and $\beta = 0°$. However, each model had its own reference area S.

Depending on the test, the pitch angles ranged as $-10° \leq \alpha \leq 10°$, and were set relative to the reference plane, which was parallel to the bottom surface of the clean fuselage. The balance was positioned on a turntable which allowed for yaw angle changes in the range $-18° \leq \beta \leq 18°$ of the tested models.

Previously obtained results in the T-1K WT were in good agreement with the T-102, T-103, T-106 and T-5 TsAGI WTs [42]. The T-1K WT results are also in good agreement with CFD computations carried out in KNRTU-KAI. The comparison of the wind tunnel results of a sample helicopter fuselage with CFD computations is shown on Figure 11. Here all drag values were scaled to the maximum C_D value ($C_D/C_{D\max}$) at $C_L = -0.3$ for the CFD case at $Re = 4.4 \times 10^6$ (based on fuselage length). The 95% confidence interval of the 8-fold experiments is indicated by the error bars. The relatively good agreement with CFD suggests that the measurements have good validity. The effect of the Reynolds nubmbers can also be seen in the CFD results; it is important to bear this in mind if the experiments are to be scaled to full-size helicopters.

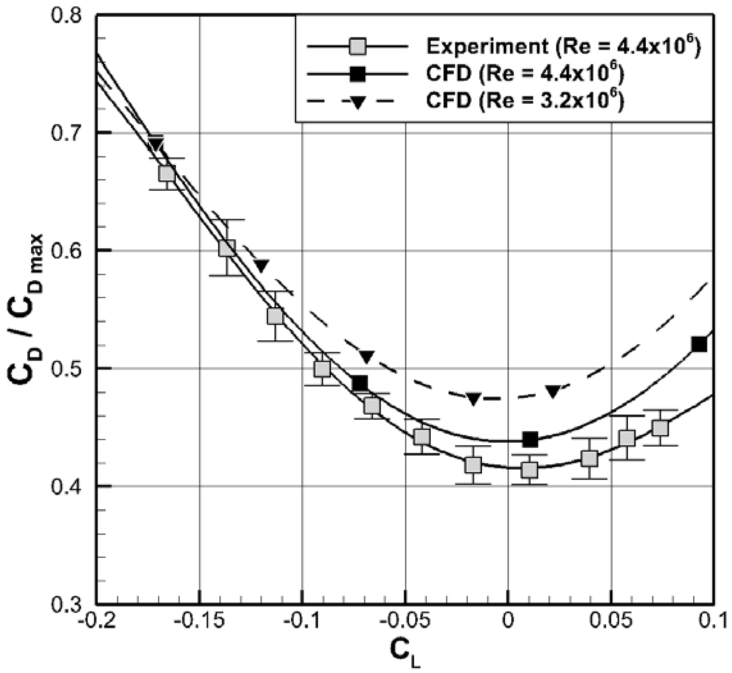

Figure 11. Comparison of experimental and CFD results of a sample helicopter fuselage [43]

3.2. Random errors

Random errors were accounted for by performing eightfold experiments at wind speed of V=36 m/s, which approximately corresponded to the range $3.6 \cdot 10^6 \leq Re \leq 4 \cdot 10^6$. Random errors depend on many factors, the main being measurement system errors, errors due to the model positioning, the unsteady character of aerodynamic loading, etc. The magnitude of random errors depends on the scale and aerodynamic properties of the tested models.

Measured samples were described by a Gaussian distribution function with mean $\bar{x}$ and standard deviation σ. The $\bar{x} \pm 1.96\sigma$ interval corresponds to a 95% confidence interval [44].

$$\bar{x} = \frac{1}{N} \sum_{i=1}^{N} x_i \tag{1}$$

$$\sigma = \sqrt{\frac{1}{\mathrm{N}-1} \sum_{i=1}^{N} (x_i - \bar{x})^2} \tag{2}$$

Here, N is the number of samples ($N = 8$ for eightfold experiments) and x_i is the i^{th} measurement.

Due to high operational costs of WTs, the eightfold confidence intervals in this paper were calculated only for cases of Models 1 and 4 (see Figures 12,17,18), which was also used as an estimate to assess errors present in the experiments. In terms of C_{DS}, the confidence intervals varied from 0.019 to 0.123.

3.3. Data presentation

3.3.1. Scaled drag coefficient

The obtained drag coefficients C_D at different pitch (α) and yaw (β) angles were scaled with a constant coefficient k_0, resulting in a scaled drag coefficient C_{DS}:

$$C_{DS} = k_0 C_D \tag{3}$$

Here, C_D is the actual drag coefficient measured during the WT experiments for a given fuselage configuration (C_D values of the different configurations were calculated based on the reference area S of the clean fuselage); the coefficient k_0 has the same value for all plots in the paper but its exact value is not disclosed.

The plot style in this work includes + and – signs, which indicate presence or absence of a fuselage component, respectively. For example, (CF4+; TP−; SK1−; FT3−) configuration indicates that the Model 4 clean fuselage (CF4) was used, and that the tailplane (TP), first configuration of skids (SK1) and the third configuration of fuel tanks (FT3) were removed.

For convenience, if the same configuration is presented on the same figure for two different models, they have same symbols but different colours (black, grey and white). For example, the (CF1+; SK1+; TP+; MH−) and (CF2+; SK1+; TP+; MH−) configurations in Figure 12 represent the same configuration for two different models. Therefore, they are indicated by same square-symbol (but with black and grey colours).

3.3.2. Calculation of the drag increase

The percentage of the drag increase for different configurations was calculated by using two values of C_{DS} for both configurations at the same angle of attack, and the following relation:

$$\Delta C_D = \frac{C_{DS_k} - C_{DS_j}}{C_{DS_j}} \cdot 100\% = \left(\frac{k_0 C_{D_k}}{k_0 C_{D_j}} - 1\right) \cdot 100\% = \left(\frac{C_{D_k}}{C_{D_j}} - 1\right) \cdot 100\% \qquad (4)$$

here,

ΔC_D	is the drag increase of the k^{th} configuration relative to the j^{th} configuration;
C_{DS_j},C_{DS_k}	are the scaled drag coefficients at a given pitch angle α_0 or yaw angle β_0 of the j^{th} and k^{th} configurations, respectively;
C_{D_j}, C_{D_k}	are the unscaled drag coefficients at a given pitch angle α_0 or yaw angle β_0 of the j^{th} and k^{th} configurations, respectively;
k_0	is a constant coefficient, which took the same value throughout this paper;
α_0,β_0	are the arbitrary pitch and yaw angles, respectively.

As an example, at $\alpha = 10°$, $C_{DS1} = 0.0707$ for (CF2+; SK1+; TP+; MH−) and $C_{DS2} = 0.1139$ for the (CF2+; SK1+; TP+; MH+) configuration of Figure 12. This means that the presence of MH results in 61% drag increase at that angle.

Drag coefficients were calculated with the reference area S at $\alpha = 0°$ and $\beta = 0°$.

Equation (4) implies that the scaled drag coefficients for two different configurations of a given model can be used to show the drag increase (or decrease) and are independent of the coefficient k_0. This feature is used in Tables 3 to 8 to show true drag variations for different configurations of the four models.

3.3.2. Calculation of the drag brakedown

The drag brakedown was calculated as:

$$\Delta C_{D0} = \frac{C_{DS_k}}{C_{DS_{j0}}} \cdot 100\% = \frac{k_0 C_{D_k}}{k_0 C_{D_j}} \cdot 100\% = \frac{C_{D_k}}{C_{D_j}} \cdot 100\% \qquad (5)$$

Here,

ΔC_{D0}	is the drag ratio (in terms of percentage) of the k^{th} configuration relative to the j^{th} configuration;
$C_{DS_{j0}}$	is the scaled drag coefficient at a given pitch angle α_0 or yaw angle β_0 for a configuration, which has highest drag;

The drag breakdown of each model was carried out with the configuration, which had the highest drag $C_{DS_{j0}}$ for that model.

4. Results and Discussion

In this section each configuration is prefixed with the model's number. For example, configuration 1-5 indicates a configuration 5 of the Model 1.

4.1. Models 1 and 2

In this section, comparison of two models with different configurations is considered. Model 2 has the same fuselage shape as Model 1, except of its extended rear ramp.

Figure 12 shows how the drag of the configurations differ with the pitch angle α. The addition of skids (SK1) from configuration 1-3 (CF1+;SK1+;TP+;MH−) to configuration 1-5 (CF1+;SK1−;TP+;MH−) resulted in a gradual increase of the drag coefficient ΔC_D from 23% at $\alpha = -10°$ to 78% at $\alpha = 10°$. Then, removal of the TP from configuration 1-3 resulted in a slight drag decrease (see configuration 1-4). Configurations 1-3 and 2-2 are similar but the latter has an extended rear ramp, and their comparison indicates that drag reduction due to extended rear ramp is highest at negative angles of attack (−21% at $\alpha = -10°$) and becomes less evident at higher pitch angles (−7% at $\alpha = 10°$). This was expected since during the experiment separation zones near the rear ramp and below the tail boom were observed using a tuft wand. The extended rear ramp had delayed flow separation.

Comparison of configurations 1-3 and 1-4 indicates that installation of the TP leads to an average drag increase of 4%.

Model 2, which had an extended rear ramp, was also used to estimate drag increase because of its installed main rotor hub and hub fairing. Comparison of configurations 2-1 and 2-2 reveals that addition of MH resulted in the drag increase from 48% at $\alpha = -10°$ to 62% for $0° \leq \alpha \leq 10°$. This indicates that the drag of the main hub is higher at positive pitch angles than at negative. The average drag increase due to addition of main hub was 59% (Table 3).

Figure 13 shows the effect of drag increase of different configurations at different yaw angles β. The addition of skids from configuration 1-5 (CF1+;SK1−;TP+;MH−) to configuration 1-3 (CF1+;SK1+;TP+;MH−) resulted in a drag increase from 36% at $\beta = -18°$ to its maximum value of 66% at $\beta = -6°$, and then a gradual decrease to 30% at $\beta = -12°$. Comparison of configurations 2-2 and 1-3 shows drag reduction due to the extended rear ramp, which is almost negligible at $\beta = -18°$, and which then gradually decreases to -16% at $\beta = 3°$, and then gradually increases to -11% at $\beta = 12°$. The difference between Model 1 and Model 2 in terms of drag reduction becomes more evident near zero yaw because of the lower form drag due to the delayed flow separation behind the extended rear ramp.

The drag increment due to the main hub of model 2 (see configurations 2-1 and 2-2) reaches its peak at near-zero yaw angles (52%) and decreases with higher (30% at $\beta = 12°$) or lower (25% at $\beta = -18°$) yaw angles.

A summary of the drag increments of the various configurations of Models 1 and 2 is presented in tables 3 and 4.

The dependence of reduced drag coefficients at different pitch angles at three different Reynolds numbers is shown in Figures 14. As can be seen, Reynolds numbers in the range $2.58 \cdot 10^6 \leq Re \leq 4.01 \cdot 10^6$ have little effect on drag, and lower drag values correspond to higher Reynolds numbers, which was expected [45].

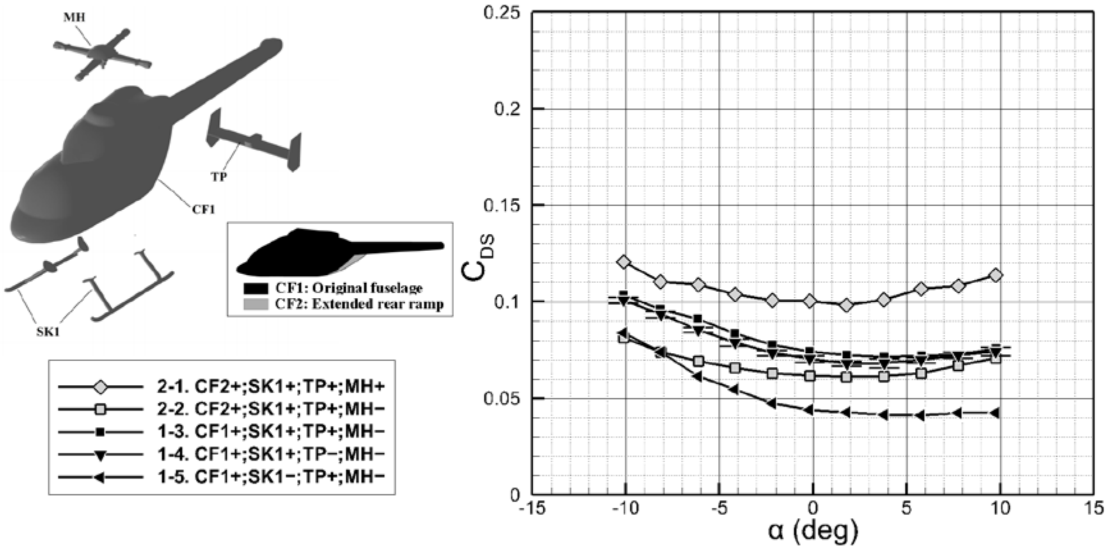

Figure 12. Models 1 and 2 (Re=3.67x10^6, M=0.1, β=0°)

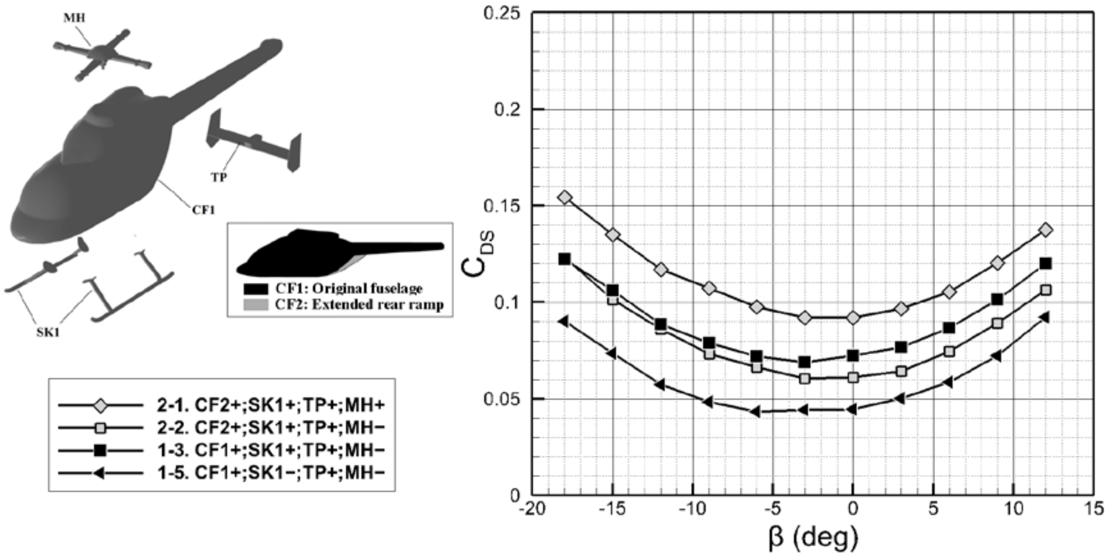

Figure 13. Models 1 and 2 (Re=3.67x10^6, M=0.1, α=0°)

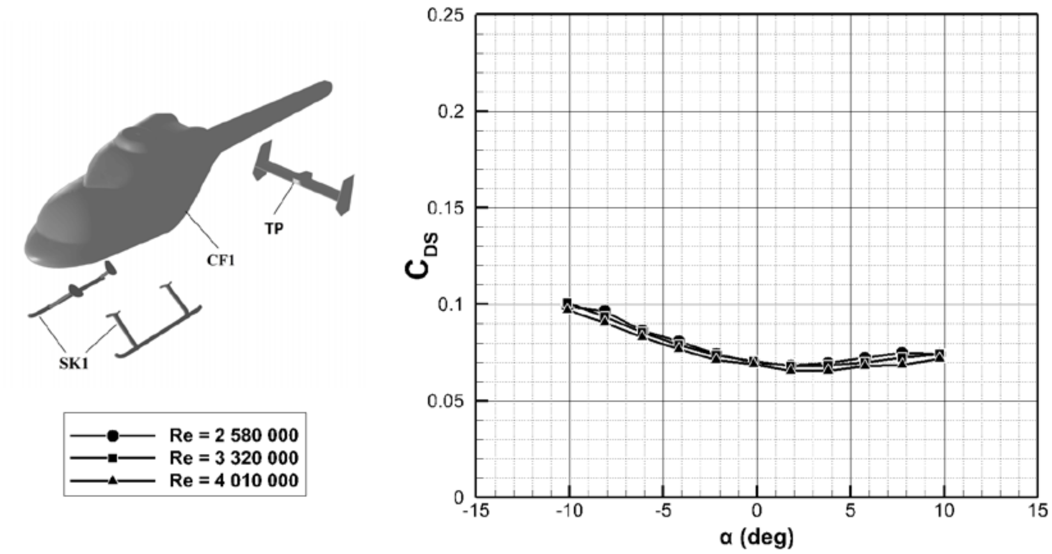

Figure 14. Model 1 (CF1+; SK1+; TP+; MH−) at different Reynolds numbers (β=0°)

	Configuration	C_{DS_j} C_{DS_k}	$\Delta C_D = \frac{C_{DS_k} - C_{DS_j}}{C_{DS_j}} \cdot 100\%$			Range of pitch angles
			min	mean	max	
From	1-5. CF1+;SK1−;TP+;MH−	j = 5	+23%	+60%	+78%	$-10° \le \alpha \le 10°$
to	1-3. CF1+;SK1+;TP+;MH−	k = 3				
From	1-4. CF1+;SK1+;TP−;MH−	j = 4	0%	+4%	+7%	$-10° \le \alpha \le 10°$
to	1-3. CF1+;SK1+;TP+;MH−	k = 3				
From	1-3. CF1+;SK1+;TP+;MH−	j = 3	−24%	−16%	−7%	$-10° \le \alpha \le 10°$
to	2-2. CF2+;SK1+;TP+;MH−	k = 2				
From	2-2. CF2+;SK1+;TP+;MH−	j = 2	+48%	+59%	+69%	$-10° \le \alpha \le 10°$
to	2-1. CF2+;SK1+;TP+;MH+	k = 1				

Table 3. Summary of the Models 1 and 2 drag increase for different configurations. Mean values are calculated over the range of pitch (α) angles.

	Configuration	C_{DS_j} C_{DS_k}	$\Delta C_D = \frac{C_{DS_k} - C_{DS_j}}{C_{DS_j}} \cdot 100\%$			Range of yaw angles
			min	mean	max	
From	1-5. CF1+;SK1−;TP+;MH−	j = 5	+30%	+50%	+66%	$-18° \le \beta \le 12°$
to	1-3. CF1+;SK1+;TP+;MH−	k = 3				
From	1-3. CF1+;SK1+;TP+;MH−	j = 3	−16%	−9%	+1%	$-18° \le \beta \le 12°$
to	2-2. CF2+;SK1+;TP+;MH−	k = 2				
From	2-2. CF2+;SK1+;TP+;MH−	j = 2	+25%	+41%	+52%	$-18° \le \beta \le 12°$
to	2-1. CF2+;SK1+;TP+;MH+	k = 1				

Table 4. Summary of the Models 1 and 2 drag increase for different configurations. Mean values are calculated over the range of yaw (β) angles.

4.2. Model 3

The tail support (TS) and main hub (MH) were installed on the clean fuselage of Model 3 for almost all tested configurations.

Figure 15 shows the effect of the pitch angle α on the drag. As can be seen, the addition of the tailplane (TP) to the configuration 3-7 (CF3+;TS+;MH+;SK2−;FT2−;TP−) results in a small drag increase, as an average value near 5% (configuration 3-6). The installation of the skids (SK2) to configuration 3-6, results in a gradual drag increase from 22% at $\alpha = -8°$ to 56% at $\alpha = 6°$ (configuration 3-4). If then external fuel tanks (FT2) are added on top of TP and SK2 to configuration 3-4 (which then becomes configuration 3-3), the drag further increases from 20% to 29% depending on the angle. However, if only skids (SK2) are added to configuration 3-7 (which is configuration 3-5), then the drag gradually increases from 20% at $\alpha = -8°$ to 55% at $\alpha = 8°$.

Comparison of configurations 3-3 and 3-4 indicates that the addition of rectangular fuel tanks (FT2) leads to 20% average drag increase over the entire range of pitch and yaw angles. In turn, addition of skids (SK2) to configuration 3-7 has an effect of about 40% drag increase and does not change over the range of yaw angles. However, the situation varies as the pitch angle changes, and the drag rises steadily from $\alpha = -8°$ to $\alpha = 8°$.

Comparison of configurations 3-1 and 3-3 indicates that FT1 is slightly better than FT2 at nonzero pitch angles. This additional drag could be due to the circular attachment rods of the FT2, which are exposed to the flow, even though FT2 is more streamlined than FT1.

Figure 16 shows the drag variation as a function of the yaw angle β. The addition of TP to the clean fuselage (i.e., to configuration 3-7), results in an insignificant drag increase; the difference can be distinguished only in the range $-6° \leq \beta \leq 12°$, where the drag increase is about 5 to 7%. On the other hand, if skids are added to configuration 3-7 (the result is configuration 3-5), the drag increases by about 41% (refer to Table 6).

The comparisons of configurations 3-6 with 3-7, 3-4 with 3-5 and 3-1 with 3-2 demonstrate that the addition of the tailplane (TP) has a very low contribution to the overall drag. Comparison of the clean fuselage configurations 3-8 and 3-7 (with installed MH and TS) indicate that MH and TS adds up 74% on average over the pitch angles and 50% over the yaw angles.

A summary of drag increments for the various configurations of Model 3 is presented in Tables 5 and 6.

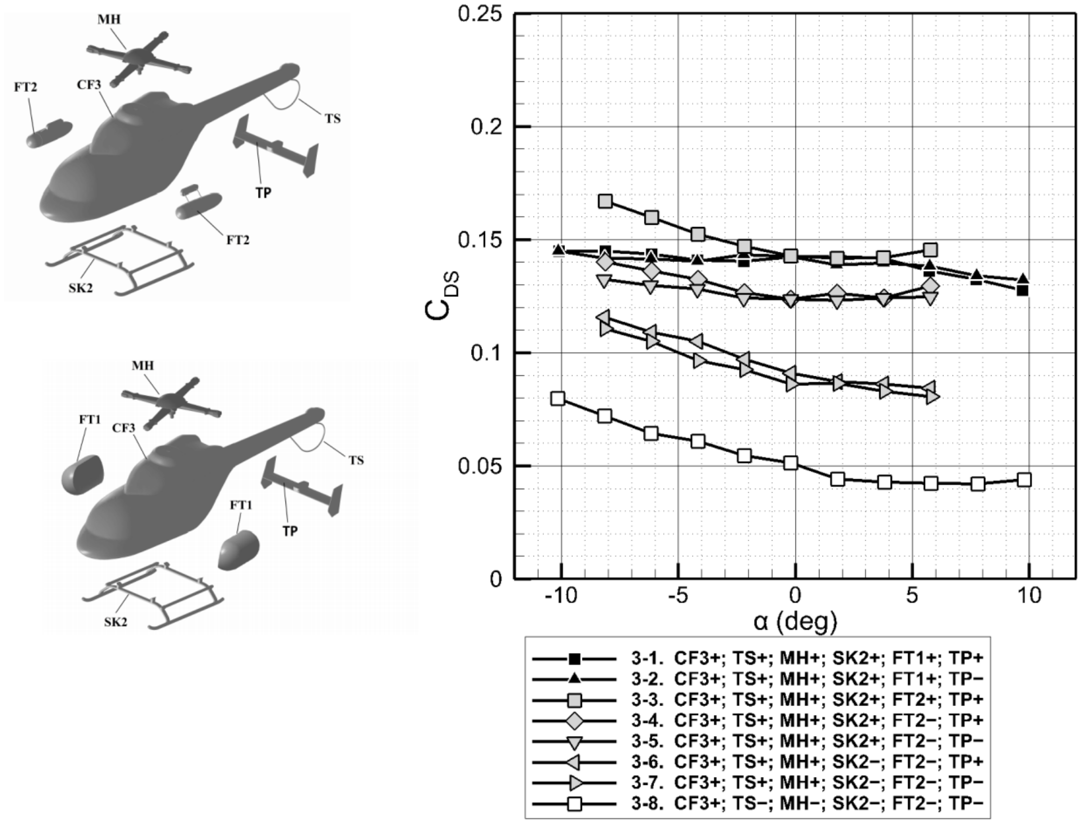

Figure 15. Model 3 (Re=3.85x10^6, M=0.1, β=0°)

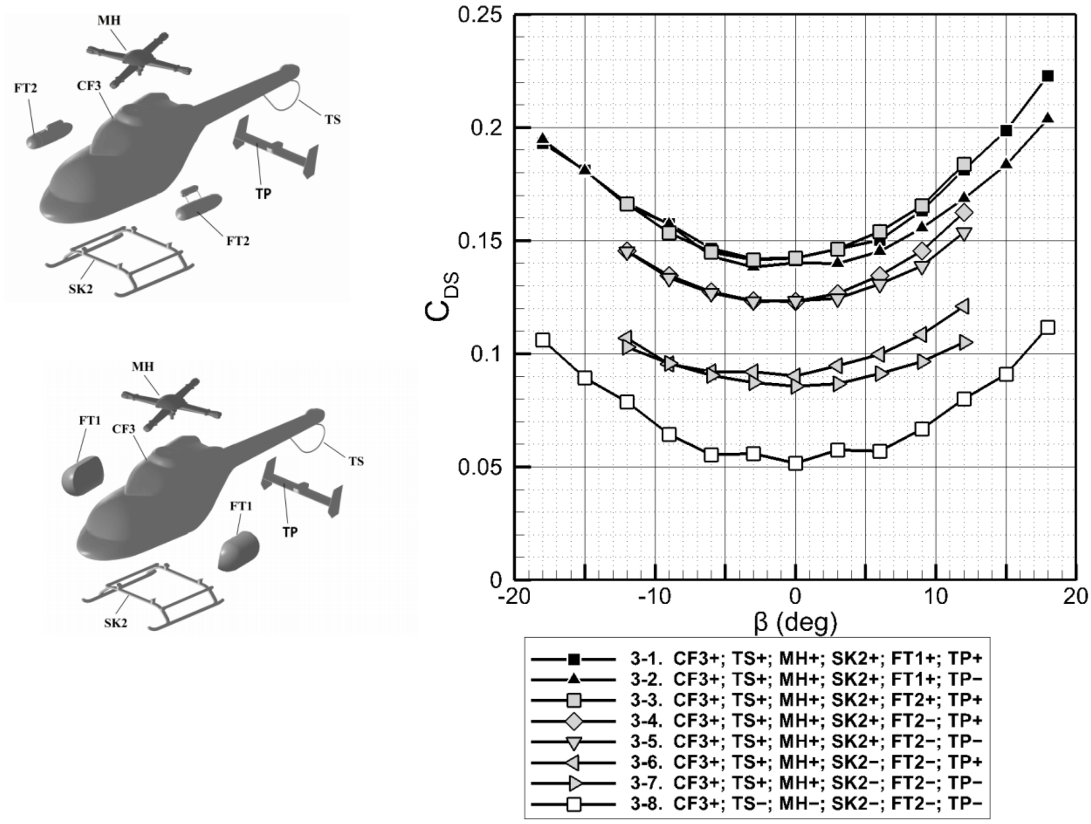

Figure 16. Model 3 (Re=3.85x10^6, M=0.1, α=0°)

	Configuration	C_{DS_j} C_{DS_k}	$\Delta C_D = \frac{C_{DS_k} - C_{DS_j}}{C_{DS_j}} \cdot 100\%$			Range of pitch angles
			min	mean	max	
From	3-7. CF3+;TS+; MH+;SK2−;FT1−;TP−	j = 7	+31%	+54%	+71%	$-8° \leq \alpha \leq 6°$
to	3-1. CF3+;TS+; MH+;SK2+;FT1+;TP+	k = 1				
From	3-7. CF3+;TS+; MH+;SK2−;FT1−;TP−	j = 7	+28%	+54%	+71%	$-8° \leq \alpha \leq 6°$
to	3-2. CF3+;TS+; MH+;SK2+;FT1+;TP−	k = 2				
From	3-7. CF3+;TS+; MH+;SK2−;FT2−;TP−	j = 7	+51%	+63%	+80%	$-8° \leq \alpha \leq 6°$
to	3-3. CF3+;TS+; MH+;SK2+;FT2+;TP+	k = 3				
From	3-7. CF3+;TS+; MH+;SK2−;FT2−;TP−	j = 7	+27%	+41%	+61%	$-8° \leq \alpha \leq 6°$
to	3-4. CF3+;TS+; MH+;SK2+;FT2−;TP+	k = 4				
From	3-7. CF3+;TS+; MH+;SK2−;FT2−;TP−	j = 7	+20%	+38%	+55%	$-8° \leq \alpha \leq 6°$
to	3-5. CF3+;TS+; MH+;SK2+;FT2−;TP−	k = 5				
From	3-7. CF3+;TS+; MH+;SK2−;FT2−;TP−	j = 7	+1%	+5%	+9%	$-8° \leq \alpha \leq 6°$
to	3-6. CF3+;TS+; MH+;SK2−;FT2−;TP+	k = 6				
From	3-8. CF3+;TS−; MH−;SK2−;FT2−;TP−	j = 8	+54%	+74%	+95%	$-8° \leq \alpha \leq 6°$
to	3-7. CF3+;TS+; MH+;SK2−;FT2−;TP−	k = 7				

Table 5. Summary of the Model 3 drag increase for different configurations. Mean values are calculated over the range of pitch (α) angles.

	Configuration	C_{DS_j} C_{DS_k}	$\Delta C_D = \frac{C_{DS_k} - C_{DS_j}}{C_{DS_j}} \cdot 100\%$			Range of pitch angles
			min	mean	max	
From	3-7. CF3+;TS+; MH+;SK2−;FT1−;TP−	j = 7	+62%	+66%	+75%	$-12° \leq \beta \leq 12°$
to	3-1. CF3+;TS+; MH+;SK2+;FT1+;TP+	k = 1				
From	3-7. CF3+;TS+; MH+;SK2−;FT1−;TP−	j = 7	+57%	+62%	+69%	$-12° \leq \beta \leq 12°$
to	3-2. CF3+;TS+; MH+;SK2+;FT1+;TP−	k = 2				
From	3-7. CF3+;TS+; MH+;SK2−;FT2−;TP−	j = 7	+59%	+64%	+69%	$-12° \leq \beta \leq 12°$
to	3-3. CF3+;TS+; MH+;SK2+;FT2+;TP+	k = 3				
From	3-7. CF3+;TS+; MH+;SK2−;FT2−;TP−	j = 7	+39%	+42%	+46%	$-12° \leq \beta \leq 12°$
to	3-4. CF3+;TS+; MH+;SK2+;FT2−;TP+	k = 4				
From	3-7. CF3+;TS+; MH+;SK2−;FT2−;TP−	j = 7	+37%	+41%	+46%	$-12° \leq \beta \leq 12°$
to	3-5. CF3+;TS+; MH+;SK2+;FT2−;TP−	k = 5				
From	3-7. CF3+;TS+; MH+;SK2−;FT2−;TP−	j = 7	+0%	+5%	+7%	$-12° \leq \beta \leq 12°$
to	3-6. CF3+;TS+; MH+;SK2−;FT2−;TP+	k = 6				
From	3-8. CF3+;TS−; MH−;SK2−;FT2−;TP−	j = 8	+31%	+50%	+66%	$-12° \leq \beta \leq 12°$
to	3-7. CF3+;TS+; MH+;SK2−;FT2−;TP−	k = 7				

Table 6. Summary of the Model 3 drag increase for different configurations. Mean values are calculated over the range of yaw (β) angles.

4.4. Model 4

In this section, comparison of different configurations of Model 4 is considered. Model 2 has the same fuselage shape as Model 1, except of its extended rear ramp. Model 4 included a tailplane (TP), type 1 skids (SK1) and type 3 fuel tanks (FT3).

Figure 17 presents the results of the experiments as function of the pitch angle (α). If TP is added to configuration 4-8 (see configuration 4-7), the drag increase remains between 11 and 15% for $-10° \leq \alpha \leq 2°$, then it gradually increases from 26–40% at higher angles. If then the rectangular fuel tanks (FT3) are added to configuration 4-7 (see configuration 4-5), the drag further increases on 30% at $\alpha = -8°$, and then gradually rises (at higher positive angles) up to 78% at $\alpha = 10°$. If skids (SK1) are added to configuration 4-5 (which then becomes configuration 4-1), the drag further rises by 30% at $\alpha = -10°$ and then gradually increases by 79% at $\alpha = 10°$.

On the other hand, if rectangular fuel tanks (FT3) are added to the clean fuselage (i.e., from configuration 4-8 to 4-6), the drag increases from 28% at $\alpha = -10°$ up to 91% at $\alpha = 10°$. If only skids (SK1, configuration 4-4) are added to the CF (configuration 4-8), then the drag rises from 27% at $\alpha = -10°$ to 148% at $\alpha = 10°$.

The addition of the TP to configuration 4-4 results in (configuration 4-3) 18% drag increase (at $\alpha = -10°$) and 3% (at $\alpha = -2°$), which then remains relatively constant at the 3% level till $\alpha = 10°$. On the other hand, the addition of the FT3 (configuration 4-2) to configuration 4-4 results in the drag increase of 21% for the $0° \leq \alpha \leq 8°$ range and a relatively constant drag increase of 30 to 32% for the remaining range.

The results of the yaw angle tests are presented in Figure 18. The addition of the TP to configuration 4-8 results in a gradual drag increase from 4% at $\beta = -15°$ to 22% at $\beta = -18°$ (see configuration 4-6). Adding the rectangular fuel tanks (FT3) (configuration 4-5) to configuration 4-6 results in additional drag rise, from 20% (at $\beta = -18°$) to 36% (at $\beta = -6°$) and back to 16% (at $\beta = 18°$). Further addition of skids to configuration 4-5 (which is configuration 4-1) increases drag between 58 and 71%.

If, on the other hand, FT3 is added to configuration 4-8 (which is configuration 4-6), the drag increases gradually from 13% (at $\beta = -18°$) to 42% (at $\beta = -3°$), and then decreases gradually to 24% (at $\beta = 18°$). If skids (SK1) are added to configuration 4-6 (the result is configuration 4-2), then an additional increase of about 60% is observed.

Additional installation of the TP (configuration 4-3) results in the gradual drag increase from 0% (at $\beta = -18°$) to 16% (at $\beta = 18°$).

Comparisons of configurations 4-1 and 4-2, 4-3 and 4-4, 4-5 and 4-6, 4-7 and 4-8 show that, in general, the TP brings an almost constant drag increase over the range of pitch and yaw angles. The drag slope configurations of skids (SK1) and fuel tanks (FT3) configurations in Figure 17 reveal that it is minimal at negative pitch angles (α), and is highest at positive pitch angles (α).

A summary of drag increments due to different configurations of Model 4 is presented in Tables 7 and 8.

The dependence of reduced drag coefficients at different pitch and yaw angles at three different Reynolds numbers is shown in Figures 19 and 20 for clean fuselage configuration. As can be seen, Reynolds numbers in this range have little effect on drag.

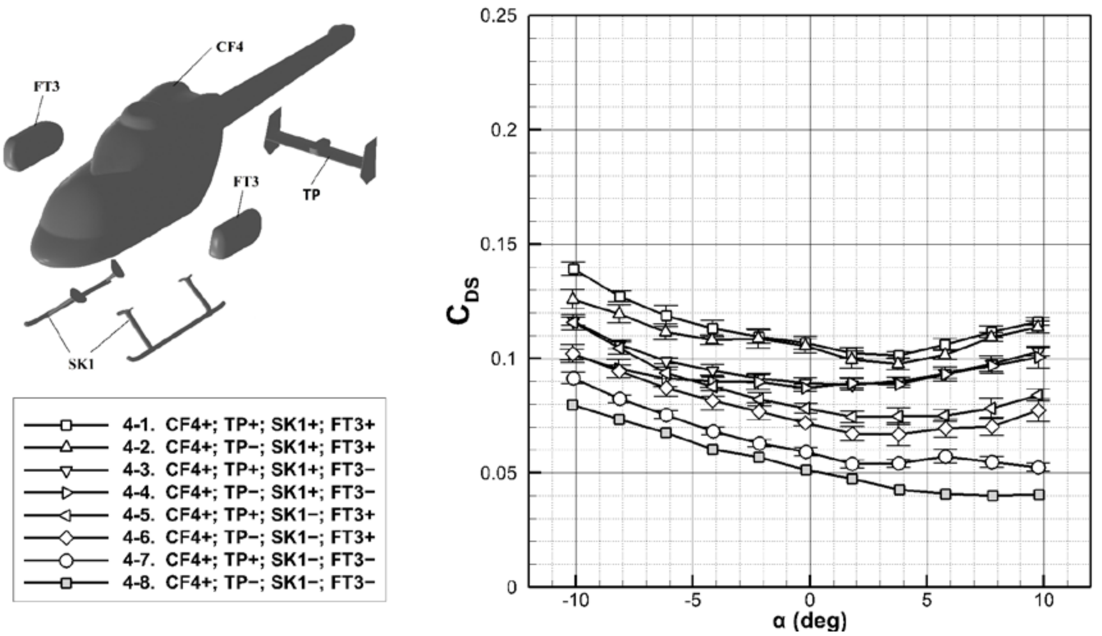

Figure 17. Model 4 (Re=3.96x10^6, M=0.1, β=0°)

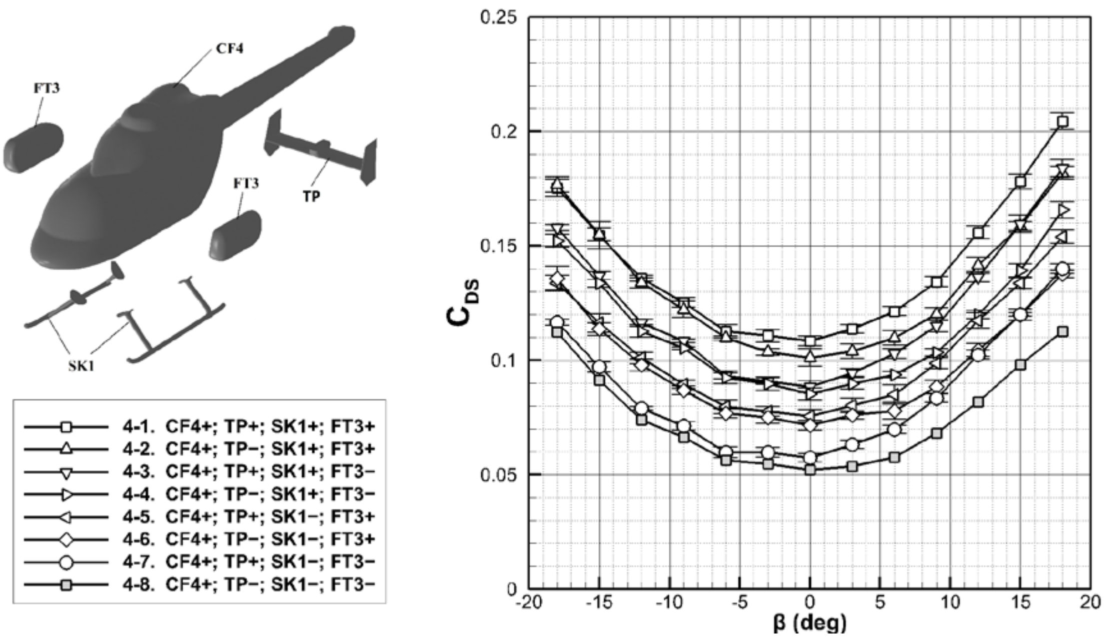

Figure 18. Model 4 (Re=3.96x10^6, M=0.1, α=0°)

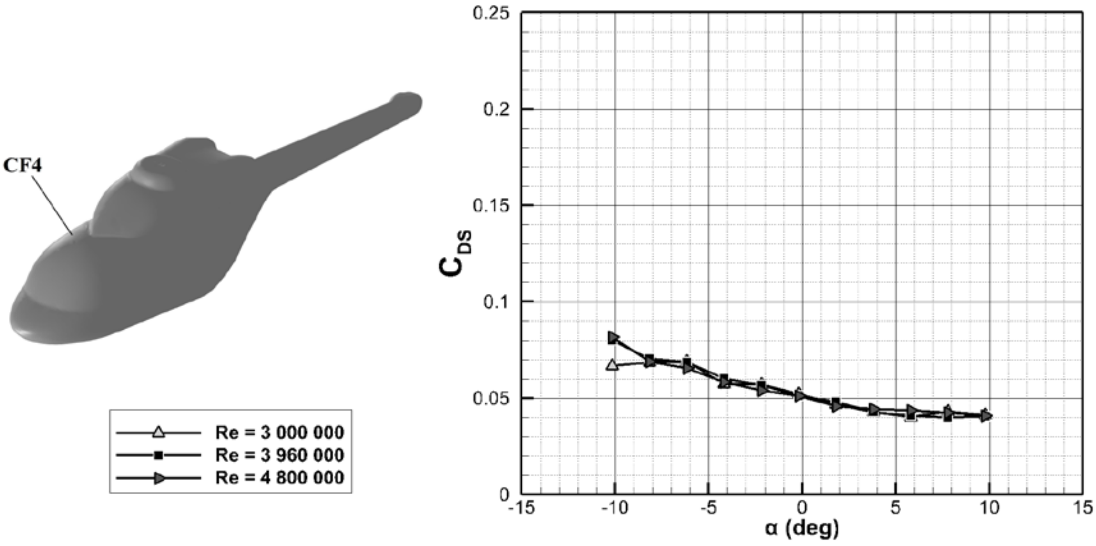

Figure 19. Model 4 at different Reynolds numbers (β=0°)

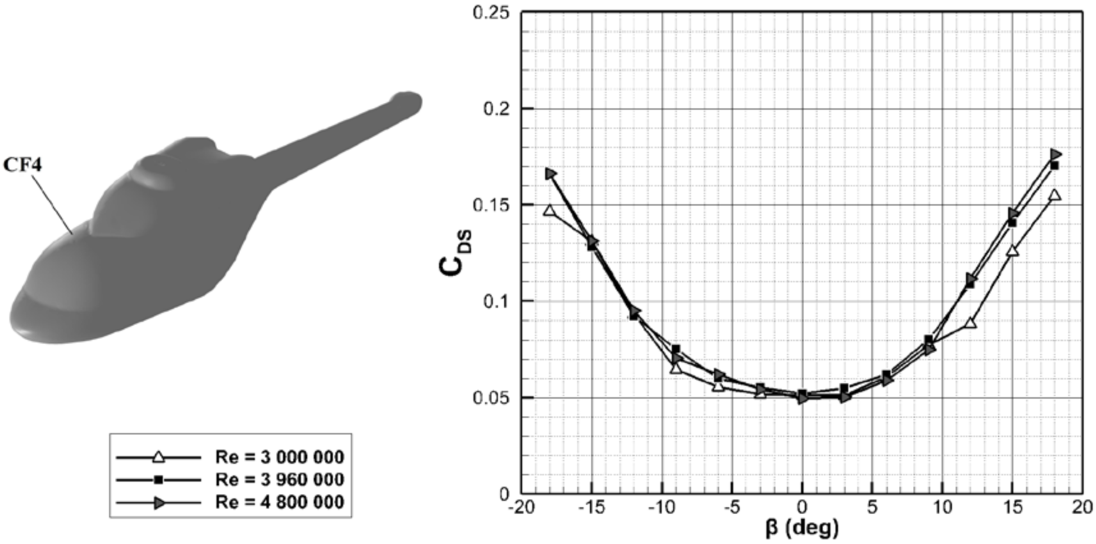

Figure 20. Model 4 at two different Reynolds numbers (α=0°)

	Configuration	C_{DS_j} C_{DS_k}	$\Delta C_D = \frac{C_{DS_k} - C_{DS_j}}{C_{DS_j}} \cdot 100\%$			Range of pitch angles
			min	mean	max	
From to	4-8. CF4+; TP−;SK1−;FT3− 4-1. CF4+; TP+;SK1+;FT3+	j = 8 k = 1	+73%	+117%	+186%	$-10° \leq \alpha \leq 10°$
From to	4-8. CF4+; TP−;SK1−;FT3− 4-2. CF4+; TP−;SK1+;FT3+	j = 8 k = 2	+58%	+109%	+180%	$-10° \leq \alpha \leq 10°$
From to	4-8. CF4+; TP−;SK1−;FT3− 4-3. CF4+; TP+;SK1+;FT3−	j = 8 k = 3	+44%	+87%	+154%	$-10° \leq \alpha \leq 10°$
From to	4-8. CF4+; TP−;SK1−;FT3− 4-4. CF4+; TP−;SK1+;FT3−	j = 8 k = 4	+27%	+80%	+148%	$-10° \leq \alpha \leq 10°$
From to	4-8. CF4+; TP−;SK1−;FT3− 4-5. CF4+; TP+;SK1−;FT3+	j = 8 k = 5	+38%	+62%	+107%	$-10° \leq \alpha \leq 10°$
From to	4-8. CF4+; TP−;SK1−;FT3− 4-6. CF4+; TP−;SK1−;FT3+	j = 8 k = 6	+28%	+48%	+91%	$-10° \leq \alpha \leq 10°$
From to	4-8. CF4+; TP−;SK1−;FT3− 4-7. CF4+; TP+;SK1−;FT3−	j = 8 k = 7	+11%	+20%	+40%	$-10° \leq \alpha \leq 10°$

Table 7. Summary of the Model 4 drag increase for different configurations. Mean values are calculated over the range of pitch (α) angles.

	Configuration	C_{DS_j} C_{DS_k}	$\Delta C_D = \frac{C_{DS_k} - C_{DS_j}}{C_{DS_j}} \cdot 100\%$			Range of yaw angles
			min	mean	max	
From to	4-8. CF4+; TP−;SK1−;FT3− 4-1. CF4+; TP+;SK1+;FT3+	j = 8 k = 1	+77%	+98%	+109%	$-18° \leq \beta \leq 18°$
From to	4-8. CF4+; TP−;SK1−;FT3− 4-2. CF4+; TP−;SK1+;FT3+	j = 8 k = 2	+79%	+86%	+94%	$-18° \leq \beta \leq 18°$
From to	4-8. CF4+; TP−;SK1−;FT3− 4-3. CF4+; TP+;SK1+;FT3−	j = 8 k = 3	+58%	+65%	+78%	$-18° \leq \beta \leq 18°$
From to	4-8. CF4+; TP−;SK1−;FT3− 4-4. CF4+; TP−;SK1+;FT3−	j = 8 k = 4	+47%	+57%	+66%	$-18° \leq \beta \leq 18°$
From to	4-8. CF4+; TP−;SK1−;FT3− 4-5. CF4+; TP+;SK1−;FT3+	j = 8 k = 5	+28%	+36%	+47%	$-18° \leq \beta \leq 18°$
From to	4-8. CF4+; TP−;SK1−;FT3− 4-6. CF4+; TP−;SK1−;FT3+	j = 8 k = 6	+17%	+29%	+41%	$-18° \leq \beta \leq 18°$
From to	4-8. CF4+; TP−;SK1−;FT3− 4-7. CF4+; TP+;SK1−;FT3−	j = 8 k = 7	+4%	+10%	+22%	$-18° \leq \beta \leq 18°$

Table 8. Summary of the Model 4 drag increase for different configurations. Mean values are calculated over the range of yaw (β) angles.

4.5. Parasite drag breakdown

In this section, the results are summarized in terms of parasite drag breakdown (with interference effects) for each model. Models 1 and 2 are considered together, because the only difference between them is the extended rear ramp of the latter. Two cases are shown for Model 3: the drag breakdown for FT1 and FT2. Model 4 is presented last.

The reference value of each model is taken as the one, having the highest average drag over the range of considered angles. The calculations are performed using Equation (5).

Figures 21-22 show the drag breakdown of Models 1 and 2. Fully dressed configuration 2-1 was taken as a reference drag value $C_{DS_{j0}}$.

The drag breakdown of the Model 3 was performed with respect to two different fuel tanks FT1 and FT2. Figures 23-24 show the results for the fuselage with FT1. The drag brakedown with respect to FT2 is presented in Figures 25-26.

The drag breakdown of the Model 4 is shown in Figures 27-28.

Finally, the summary of obtained drag values, averaged over the range of pitch (α) and yaw (β) angles, is presented in Table 9.

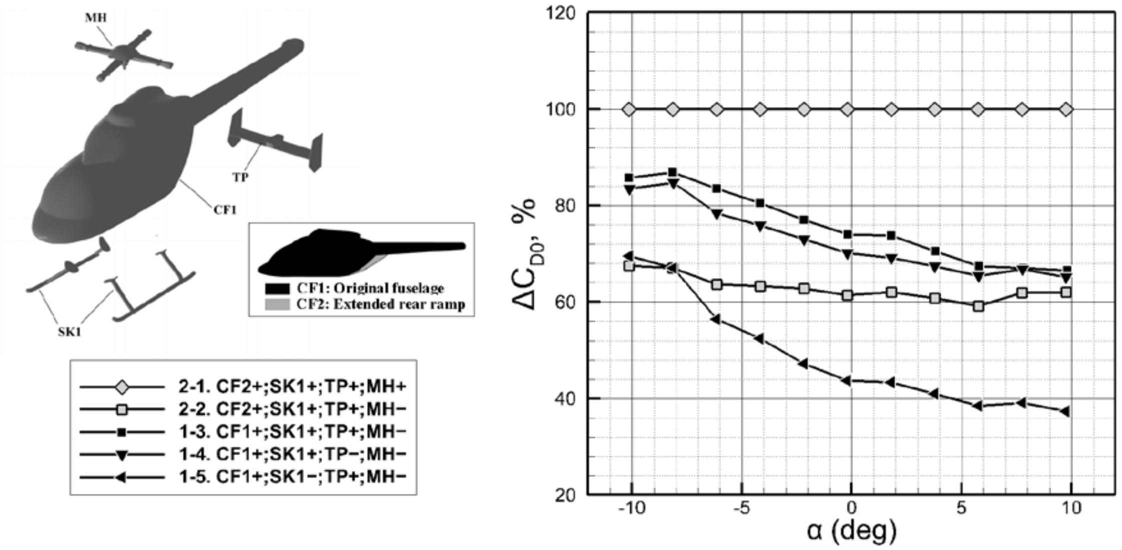

Figure 21. Parasite drag breakdown of Models 1 and 2 with respect to configuration 2-1 (Re=3.67x10^6, M=0.1, β=0°)

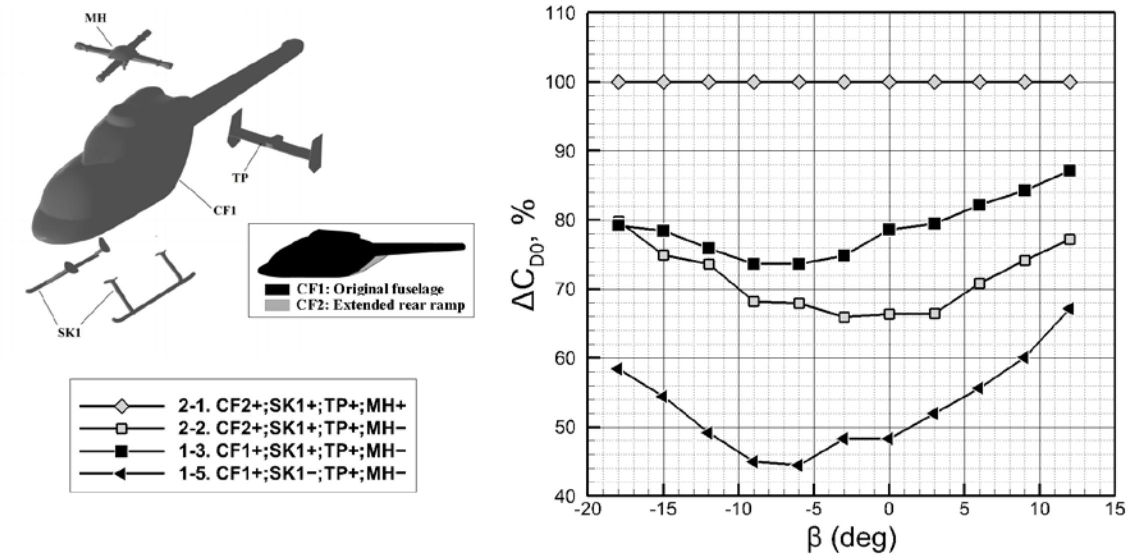

Figure 22. Parasite drag breakdown of Models 1 and 2 with respect to configuration 2-1 (Re=3.67x10^6, M=0.1, α =0°)

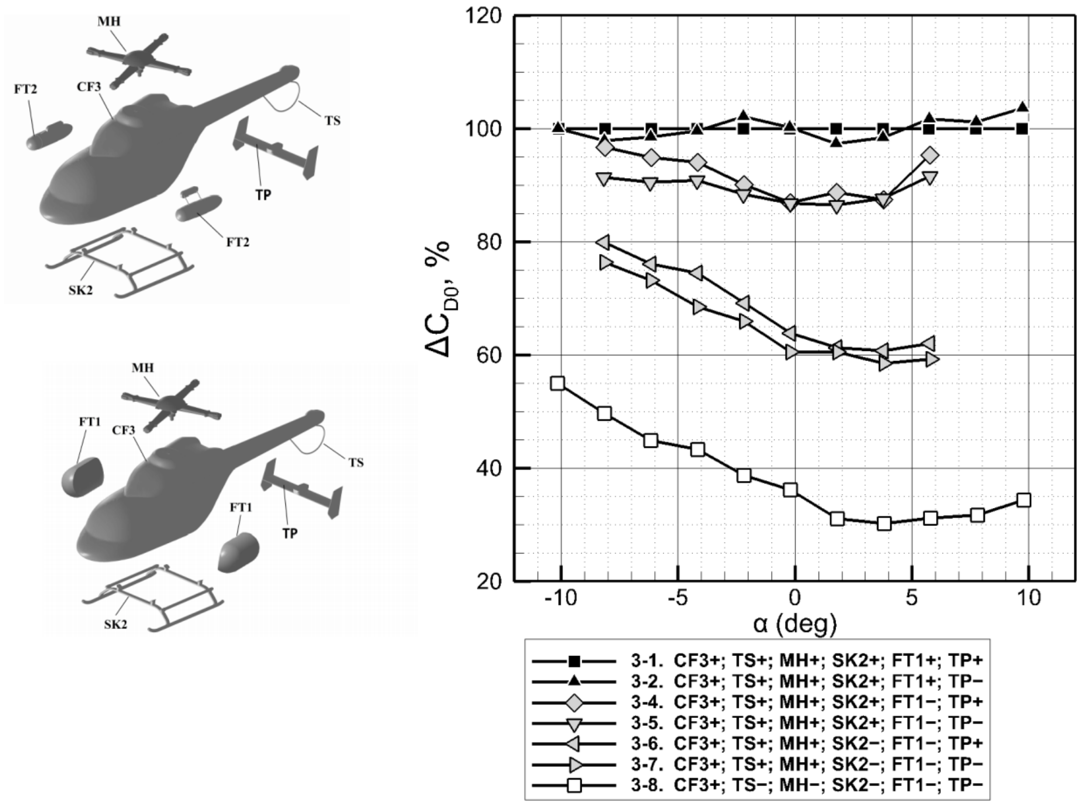

Figure 23. Parasite drag breakdown of Model 3 with respect to configuration 3-1 with FT1 (Re=3.85x10^6, M=0.1, β =0°)

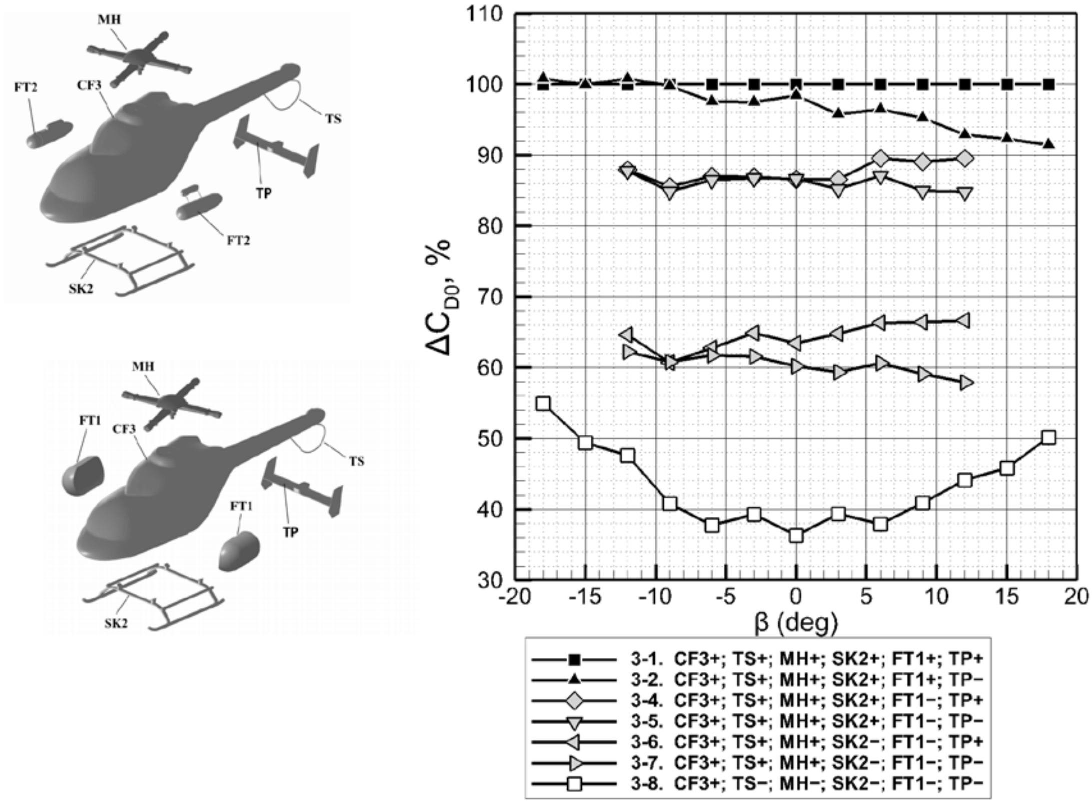

Figure 24. Parasite drag breakdown of Model 3 with respect to configuration 3-1 with FT1 (Re=3.85x10^6, M=0.1, α =0°)

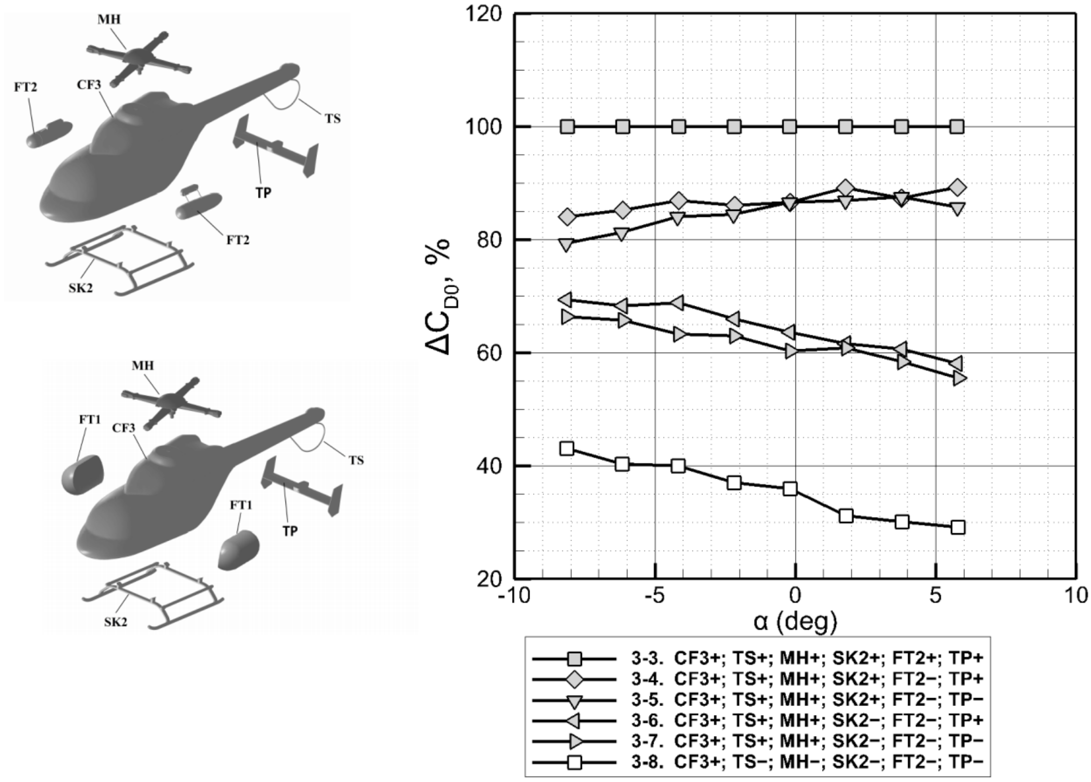

Figure 25. Parasite drag breakdown of Model 3 with respect to configuration 3-3 with FT2 (Re=3.85x10^6, M=0.1, β =0°)

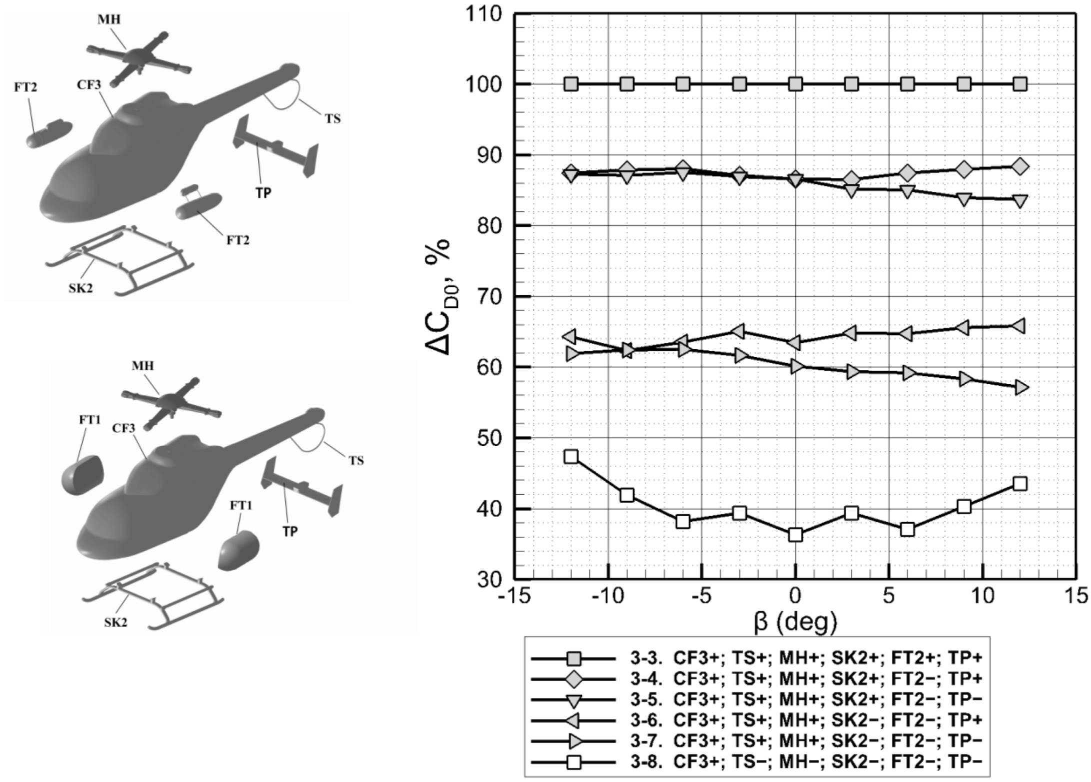

Figure 26. Parasite drag breakdown of Model 3 with respect to configuration 3-3 with FT2 (Re=3.85x10^6, M=0.1, α =0°)

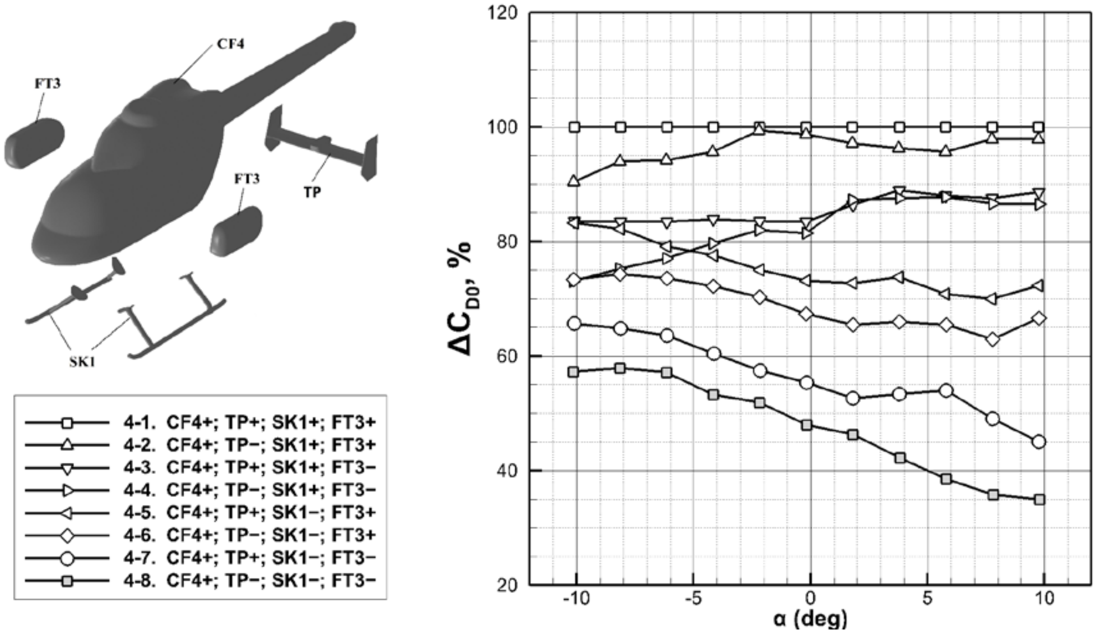

Figure 27. Parasite drag breakdown of Model 4 with respect to configuration 4-1 ($Re=3.96x10^6$, M=0.1, β =0°)

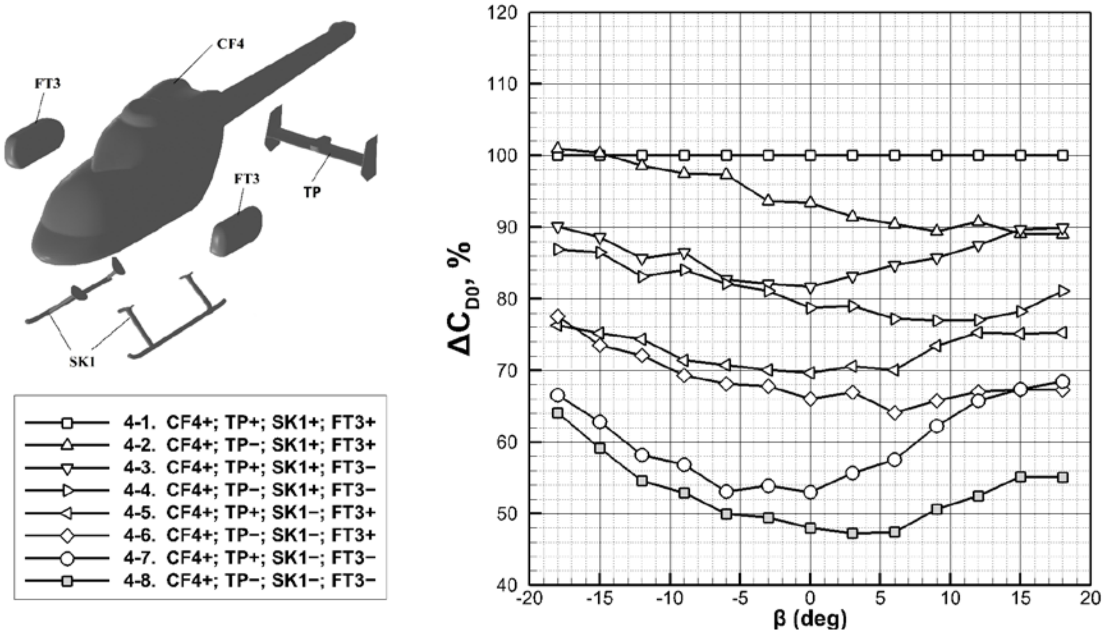

Figure 28. Parasite drag breakdown of Model 4 with respect to configuration 4-1 ($Re=3.96x10^6$, M=0.1, α =0°)

	Configuration	$-10° \leq \alpha \leq 10°$	$-18° \leq \beta \leq 12°$
Models 1, 2	2-1. CF2+;SK1+;TP+;MH+	100%	100%
	1-4. CF1+;SK1+;TP−;MH−	73%	-
	1-3. CF1+;SK1+;TP+;MH−	76%	79%
	2-2. CF2+;SK1+;TP+;MH−	63%	72%
	1-5. CF1+;SK1−;TP+;MH−	49%	54%
Model 3 (FT1)	Configuration	$-8° \leq \alpha \leq 6°$	$-12° \leq \beta \leq 12°$
	3-1. CF3+;TS+; MH+;SK2+;FT1+;TP+	100%	100%
	3-2. CF3+;TS+; MH+;SK2+;FT1+;TP−	99%	97%
	3-4. CF3+;TS+; MH+;SK2+;FT1−;TP+	92%	88%
	3-5. CF3+;TS+; MH+;SK2+;FT1−;TP−	84%	86%
	3-6. CF3+;TS+; MH+;SK2−;FT1−;TP+	68%	65%
	3-7. CF3+;TS+; MH+;SK2−;FT1−;TP−	65%	60%
	3-8. CF3+;TS−; MH−;SK2−;FT1−;TP−	38%	41%
Model 3 (FT2)	Configuration	$-8° \leq \alpha \leq 6°$	$-12° \leq \beta \leq 12°$
	3-3. CF3+;TS+; MH+;SK2+;FT2+;TP+	100%	100%
	3-4. CF3+;TS+; MH+;SK2+;FT2−;TP+	87%	88%
	3-5. CF3+;TS+; MH+;SK2+;FT2−;TP−	80%	86%
	3-6. CF3+;TS+; MH+;SK2−;FT2−;TP+	65%	64%
	3-7. CF3+;TS+; MH+;SK2−;FT2−;TP−	62%	60%
	3-8. CF3+;TS−; MH−;SK2−;FT2−;TP−	36%	41%
Model 4	Configuration	$-10° \leq \alpha \leq 10°$	$-18° \leq \beta \leq 18°$
	4-1. CF4+; TP+;SK1+;FT3+	100%	100%
	4-2. CF4+; TP−;SK1+;FT3+	96%	94%
	4-3. CF4+; TP+;SK1+;FT3−	85%	87%
	4-4. CF4+; TP−;SK1+;FT3−	82%	81%
	4-5. CF4+; TP+;SK1−;FT3+	76%	73%
	4-6. CF4+; TP−;SK1−;FT3+	69%	69%
	4-7. CF4+; TP+;SK1−;FT3−	57%	61%
	4-8. CF4+; TP−;SK1−;FT3−	48%	53%

Table 9. Parasite drag breakdown in terms of total parasite drag for each tested model. The values are averaged for the range of pith (α) and yaw (β) angles. MH was static.

5. Conclusions and Future Work

The results of wind tunnel experiments on four helicopter fuselage models has been presented. The drag increase because of the presence of skids, fuel tanks, tailplane, rotor hub, and tail support was presented.

The following conclusions were drawn:

1. Comparison of Models 1 and 2 revealed that the average drag reduction due to extended rear ramp was about 16% for pitch angles ($-10° \leq \alpha \leq 10°$) and 9% for yaw angles ($-18° \leq \beta \leq 12°$).

2. The extended rear ramp yields major benefits in terms of drag reduction at near zero yaw angles (β) and at negative pitch angles (α), where the drag decrease is mainly associated with lower values of form drag because of delayed flow separation behind the rear ramp, which was observed with the tuft wand.

3. The average value of the drag increase due to addition of the main hub to the Model 2 was 59% for $-10° \leq \alpha \leq 10°$ and 41% for $-18° \leq \beta \leq 12°$. Higher values of drag increase were observed at positive pitch angles and at close-to-zero yaw angles.

4. The addition of the twin-fin tailplane below the tail boom had low contribution to the overall drag. The addition of the tailplane was associated with almost constant drag increase over the range of pitch (α) and yaw (β) angles.

5. Almost all tests for Model 3 were carried out with the tail support and main hub. It was found that they added about 74% and 50% to the clean fuselage configuration over the range of pitch and yaw angles, respectively.

6. Two types of skids were tested with different models. Addition of the second type of skids (SK2) to the bare fuselage of Model 3 (with the tail support and with main hub) indicated at 38% drag increase over the range of pitch angles ($-8° \leq \alpha \leq 6°$). Addition of the first type of skids (SK1) to the bare fuselage of Model 4 showed an average value 80% drag increase over the range of pitch angles ($-10° \leq \alpha \leq 10°$).

7. First type of fuel tanks (FT1) were slightly better in terms of lower drag at nonzero pitch angles (α) than the second fuel tanks (FT2), which had circular attachment rods exposed to the flow.

Future studies aimed at predicting the parasite drag due to different fuselage configurations (skids, tailplane, fuel tanks, etc.), which will be based on additional experimental results, are planned in the near future.

Acknowledgements

This work was supported by the grant ‘State tasks in the field of scientific activity’ (No. 9.1694.2014 / K) of the Ministry of Education and Science of the Russian Federation.

References

[1] J. Gordon Leishman, "*Principles of Helicopter Aerodynamics,*" 2nd ed., Cambridge University Press, 2006. ISBN 9780521858601.

[2] Biava, M., Khier, W., and Vigevano, L., "CFD prediction of air flow past a full helicopter configuration," *Aerospace Science and Technology*, Vol. 19, No. 1, 2012, pp. 3–18. doi: 10.1016/j.ast.2011.08.007

[3] De Gregorio, F., "Flow field characterization and interactional aerodynamics analysis of a complete helicopter," *Aerospace Science and Technology,* Vol. 19, No. 1, 2012, pp. 19–36. doi:10.1016/j.ast.2011.11.002

[4] Renaud, T., Le Pape, A., Péron, S., "Numerical analysis of hub and fuselage drag breakdown of a helicopter configuration," *CEAS Aeronautical Journal*, Vol. 4, No. 4, 2013, pp. 409–419. doi:10.1007/s13272-013-0081-0

[5] Renaud, T., O'Brien, D., Smith, M., Potsdam, M., "Evaluation of Isolated Fuselage and Rotor-Fuselage Interaction Using Computational Fluid Dynamics," *Journal of the American Helicopter Society*, Vol. 53, No. 1, 2008, pp. 3–17. doi:10.4050/JAHS.53.3

[6] Le Chuiton, F., D'Alascio, A., Barakos, G., Steijl, R., Schwamborn, D, Lüdeke, H., "Computation of the Helicopter Fuselage Wake with the SST, SAS, DES and XLES Models," in Peng, S.-H., and Haase, W., *Advances in Hybrid RANS-LES Modelling*, Volume 97 of Notes on Numerical Fluid Mechanics and Multidisciplinary Design, pp. 117–124. Springer Berlin / Heidelberg, 2008. doi: 10.1007/978-3-540-77815-8_12

[7] Grawunder, M., Reß, R., Breitsamter, C., Adams, N.A., "Flow characteristics of a helicopter fuselage configuration including a rotating rotor head," *28th Congress of the International Council of the Aeronautical Sciences 2012, ICAS 2012*, Vol. 2, 2012, pp. 1428–1441.

[8] Khier, W., "Numerical analysis of hub and fuselage interference to reduce helicopter drag," *38th European Rotorcraft Forum 2012, ERF 2012*, Vol. 2, 2012, pp. 1200–1218.

[9] Renaud, T., Le Pape, A., and Peron, S., "Numerical analysis of hub and fuselage drag breakdown of a helicopter configuration," *CEAS Aeronautical Journal*, Vol. 4, No. 4, 2013, pp. 409–419. doi: 10.1007/s13272-013-0081-0

[10] J. Seddon and S. Newman, *Basic Helicopter Aerodynamics*, 3rd ed., Wiley, UK, 2011. ISBN 9780470665015.

[11] Prouty, R.W., *Helicopter Performance, Stability, and Control*, Krieger Publishing Company, Malabar, Florida, 2001. ISBN 1575242095.

[12] Wagner SN., "Problems of estimating the drag of a helicopter. Aerodynamic Drag," *AGARD Conference Proceedings*, 1973, No. 124, pp.5-1-10.

[13] Keys, C. N., and Wiesner, R., "Guidelines for Reducing Helicopter Parasite Drag," *Journal of the American Helicopter Society*, Vol. 20, No. 1, 1975, pp. 31–40. doi: 10.4050/JAHS.20.31

[14] Filippone, A., "Data and performances of selected aircraft and rotorcraft," *Progress in Aerospace Sciences*, Vol. 36, No. 8, 2000, pp. 629–654.

doi: 10.1016/S0376-0421(00)00011-7

[15] Hefner, J.N., Bushnell, D.M., “An overview of concepts for aircraft drag reduction”. Special Course on Concepts for Aircraft Drag Reduction, AGARD R-654. 1977.

[16] Costes, M., Renaud, T., Rodriguez, B., “Rotorcraft simulations: a challenge for CFD,” *International Journal of Computational Fluid Dynamics*, Vol. 26, No. 6–8, 2012, pp.383–405.
doi: 10.1080/10618562.2012.726710.

[17] Ewald, B.F.R. "Wind tunnel Wall Corrections". AGARD / North Atlantic Treaty Organization (NATO), 1998. ISBN-10: 9283610768.

[18] Haines A.B., “Scale effects on aircraft and weapon aerodynamics,” AGARD AG 323, July 1994.

[19] Stroub, R. H., and Rabbott, J. P. Jr., “Wasted Fuel – Another Reason for Drag Reduction,” *31st Annual National Forum of the American Helicopter Society*, Washington, D.C., May 1975, pp. 1–6.

[20] Kneisch, T., Krauss, R., D'Alascio, A., and Schimke, D., “Optimised rotor head design for an Economic Helicopter,” *37th European Rotorcraft Forum*, September 13–15, 2011. MAGA Gallarate (VA) – Italy.

[21] Sheehy, T.W., Clark, D.R., "A Method for Predicting Helicopter Hub Drag," USA AMRDL TR 75-48, 1976.

[22] Steijl, R., and Barakos, G.N., “CFD analysis of complete helicopter configurations - Lessons learnt from the GOAHEAD project,” *Aerospace Science and Technology*, Vol. 19, No. 1, 2012, pp.

.

[24] Filippone, A., and Michelsen, J.A., “Aerodynamic drag prediction of helicopter fuselage,” *Journal of Aircraft*, Vol. 38, No. 2, 2001, pp. 326–333.
doi: 10.2514/2.2765

[25] Costes, M., von Geyr, H., Collercandy, R., Kroll, N., Renzoni, P., Amato, M., Kokkalis, A., Rochetto, A., Serr, C., Larrey, E., Filippone, A., and Wehr, D., “Computation of Helicopter Fuselage Aerodynamics Using Navier-Stokes CFD Methods,” *Journal of the American Helicopter Society*, Vol. 45, No. 3, 2000, pp. 147–156.
doi: 10.4050/JAHS.45.147

[26] Gleize, V., and Costes, M., "Low-Mach-Number Preconditioning Applied to Turbulent Helicopter Fuselage Flowfield Computation ," *AIAA Journal*, Vol.41, No. 4, 2003. Pp.653–662.
doi: 10.2514/2.1995

[27] Beaumier, P., and Bousquet, J.M., "Applied CFD for Analyzing Aerodynamic Flows around Helicopters," *24th Congress of International Council of the Aeronautical Sciences*, 29 2004, Yokohama, Japan

[28] Lehmann, R. and Reddy, R. and Armfield, S., "Numerical and experimental investigation of helicopter fuselage aerodynamics," *17th Australasian Fluid Mechanics Conference,* Australia, Auckland, *2010*, pp. 27–30.

[29] Zhang, Q., Garavello, A., D'Alascio, A., Schimke, D., "Advanced CFD-based Optimization Methods Applied to the Industrial Design Process of Airframe Components at Airbus Helicopters," *37th European Rotorcraft Forum*, Gallarate, Italy, September 13-15, 2011.

[30] Seddon, J., "Aerodynamics of the helicopter rear fuselage upsweep," 8th *European Rotorcraft Forum (ERF)*, 1982.

[31] Venturelli, G., Ponza, R., and Benini, E., "Helicopter fuselage aerodynamic data fitting using multivariate smoothing thin plate splines," *Proceedings of the Institution of Mechanical Engineers, Part G: Journal of Aerospace Engineering*, Vol. 228, No. 3, 2014, pp. 384–397.

[32] Van Dam, C.P., "Recent experience with different methods of drag prediction," *Progress in Aerospace Sciences*, Vol. 35, No. 8, 1999, pp. 751–798.
doi: 10.1016/S0376-0421(99)00009-3

[33] Le Pape, A., Lienard, C., Verbeke, C., Pruvost, M., and De Coninck, J., "Helicopter Fuselage Drag Reduction Using Active Flow Control: a Comprehensive Experimental Investigation," *American Helicopter Society 69th Annual Forum*, Phoenix, Arizona, USA, 2013. Paper 132.
doi: 10.4050/JAHS.60.032003

[34] Schaeffler, N. W., Allan, B. G., Wong, O. D., and Tanner, P. E., "Experimental Investigation of Active Aerodynamic Load Reduction on a Rotorcraft Fuselage with Rotor Effects," *32nd AIAA Applied Aerodynamics Conference*, Vol. 3, Atlanta, Georgia, USA, 16-20 June, 2014.
doi: 10.2514/6.2014-2561

[35] Martin, P.B., Overmeyer, A.D., Philip E. Tanner, Wilson, J.S., and Jenkins, L.N., "Helicopter Fuselage Active Flow Control in Presence of a Rotor," *70th Annual National Forum of the American Helicopter Society*, Paper 335, Montreal, Quebec, Canada, 2014.

[36] Renaud, T., O'Brien, D., Smith, M., and Potsdam, M., "Evaluation of isolated fuselage and rotor-fuselage interaction using computational fluid dynamics," *Journal of the American Helicopter Society*, Vol. 53, No. 1, 2008, pp. 3–17.
doi: 10.4050/JAHS.53.3

[37] Boelens, O.J., van der Ven, H., Kok, J.C., Barakos, G., Biava, M., Brocklehurst, A., Costes, M., D'Alascio, A., Dietz, M., Drikakis, D., Ekaterinaris, J., Humby, I., Khier, W., Knutzen, B., LeChuiton, F., Pahlke, K., Renaud, T., Schwarz, T., Steijl, R., Sudre, L., Vigevano, L., Zhong, B., "Aerodynamic simulation of a complete helicopter configuration. The blind test activity of the GOAHEAD project." Report no. NLR-TP-2007-604.

[38] Reß, R., Grawunder, M., and Breitsamter, Ch., "Aerodynamic Analysis of a Helicopter Fuselage With Rotating Rotor Head," *Progress in Flight Physics*, 2015, Vol. 7, pp.99-110.

[39] Hoerner, S.F., *Fluid Dynamic Drag: Practical Information on Aerodynamic Drag and Hydrodynamic Resistance*, Hoerner Fluid Dynamics,++ 1965. ISBN-13 978-9991194448.

[40] Zherekhov, V.V., Pakhov, V.V. , "Automatical Measuring System of T-1K Wind Tunnel for Integral Aerodynamic Coefficients Calculation," *XXth international Chatayev conference proceedings*, Kazan, June 12–16, 2015. Vol. 1, pp. 161–168. In Russian. ISSN 987-5-7579-1730-6.

[41] Smirnova, S.I., Pakhov, V.V., Stepanov, R.P., Zherekhov, V.V., Barakos, G., "Estimation and Minimization of Influence of Various Supports on Integral Aerodynamic Characteristics of Axisymmetric Bodies and Isolated Helicopter Fuselages in the Low-Speed Wind Tunnel," *Trudy MAI*, Vol.73, pp.1–20, In Russian. ISSN 1727-6942.

[42] Zherekhov, V.V., Ledyankina, O.A., "Half-Model Method Application for Low-Speed Wind Tunnel," *XXth international Chatayev conference proceedings*, Kazan, June 12–16, 2015. Vol. 1. pp. 154-160. In Russian. ISSN 987-5-7579-1730-6.

[43] Batrakov, A., Garipova, L., Kusyumov, A., Mikhailov, S., and Barakos, G., "Computational Fluid Dynamics Modeling of Helicopter Fuselage Drag," *Journal of Aircraft*.
doi: 10.2514/1.C033019.

[44] Bonamente, M., "*Statistics and Analysis of Scientific Data*," 2013. Springer, *Graduate Texts in Physics* series. ISBN 978-1-4614-7984-0.

[45] Schlichting, H., *Boundary-Layer Theory*."1979, McGrow-Hill, 7th ed. ISBN 0-07-055334-3.